POLITECNICO DI TORINO

SCUOLA DI DOTTORATO
Dottorato in Ingegneria Aerospaziale – XXVI ciclo

Tesi di Dottorato

Multiscale approaches for the failure analysis of fiber-reinfoced composite structures using the 1D CUF

Marianna Maiarù

Tutore
Prof. Erasmo Carrera
Prof. Anthony M. Waas
Dr. Marco Petrolo

Coordinatore del corso di dottorato

Prof.ssa Fulvia Quagliotti

Aprile 2014

To my father

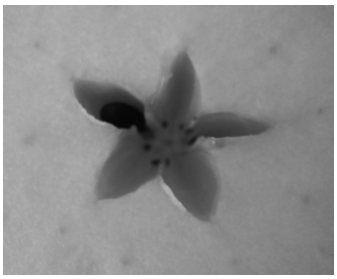

Acknowledgements

I would like to thank my advisor, professor Erasmo Carrera, for his guidance in carrying out this research project. The appreciation for his work and his passion for the research activities have been the leading reasons to join the Ph.D. program at the Politecnico di Torino, his advices on both my research and my career have been priceless.
I am also extremely appreciative for the useful and constructive recommendations of professor Anthony M. Waas at the University of Michigan. It was a great honor to be part of the Composite Structure Lab for completing my thesis and I am proud to be a current member of the group today.
I am very grateful to Dr. Marco Petrolo for his valuable suggestions during the planning and development of this research work. I learned a lot from his great example and excellent skills in organizing.
Also I would like to express all my appreciation to Pascal Meyer for his cooperation during the time spent at the University of Michigan. His experience in multiscale and failure analysis have been precious for this work and his friendship is important to me.
Special thanks are for the members of the MUL2 group and my colleagues at the Politecnico: Enrico Zappino, Alberto Varello, Alfonso Pagani, Matteo Filippi, Alessandro Lamberti, Tommaso Cavallo, Stefano Valvano and Francesco Zangallo, Salvatore Brischetto with whom I shared three intense and productive years. In particular from the Mul2 team, I want to acknowledge Mirella Cinefra for being a supportive colleague and a very good friend and Federico Miglioretti with whom I shared my best times at the Politecnico. Thanks to Pietro Nali and Gaetano Giunta, two very important people at the beginning of my Ph.D. program. My gratitude also goes to Alessandra Dal Bianco and Costantino Sardu for being such a good office mates and Matteo Orazi whose support and friendship are among the best things I will remember of this last three years.
Also I am very grateful to Dr. Royan D'Mello, Jiawen Xie, Brian Justusson, Ashith Joseph, Dr. Dianyun Zhang, and Bertram Stier for the good time together. Assistance and care provided by Anne Lee Rhoades were greatly appreciated.
Last but not least at all, thanks to the people who made this work possible, my family, my friends and Salvatore.

Summary

Composites provide significant advantages in performance, efficiency and costs; thanks to these features, their application is increasing in many engineering fields, such as aerospace, naval and mechanical engineering. Although the adoption of composites is rising, there are still open issues to be investigated, in particular, understanding their failure mechanism has a prominent role in enhancing component designs. Fiber reinforced composite structures are built using laminates composed by different layers with different fiber orientations; for this reason their behavior is characterized by different length scales in the sub-lamina (fiber and matrix), the ply and the whole laminate characteristic dimensions. The proper modeling of these scales and of their interactions is of primary importance to detect reliable stress fields and to evaluate the structural integrity of a composite structure. Indeed, many micromechanical effects have to be taken into account to evaluate the different possible failure modes. Numerous methodologies are available to compute accurate stress/strain fields for laminated structures, multi-scale approaches are required when micro- and macro-scales are accounted for. Despite the increasing development in computer hardware, the computational effort of these methods is still prohibitive for extensive applications, especially when a high number of layers is considered. Then, the reduction of the computational time and cost required to perform failure analysis is still a challenging task.

This work proposes a novel approach for the FE analysis of fiber-reinforced composites which is able to provide accurate stress and strain fields with very low computational costs using 1D refined theories. The structural models are derived in the framework of the Carrera Unified Formulation (CUF) which provides hierarchical higher-order structural models with arbitrary expansion orders where the order of the unknown variables over the cross-section is a free parameter of the formulation. Taylor- and Lagrange-type polynomials are used to interpolate the displacement field over the element cross-section. The 1D CUF formulation is herein exploited to develop two multi-scale approaches, respectively a concurrent method and a hierarchical technique. The proposed novel concurrent approach is referred to as *Component-Wise* (CW). Within the CW approach, different scale components (fiber, matrix, laminae and laminates) can be simultaneously modelled with separate sets of unknown displacement variables and material characteristics. That is, in a given model homogenized laminates or laminae can be interfaced with fiber and matrix portions. This method permits us to tune the model capabilities by choosing in which portion of the structure a more detailed model has to be used and setting the order of the

structural model to be considered. In the CW approach, a single fiber/matrix cell is considered the simplest assessment for the analysis. Cells can be opportunely included in more complex structural configurations to refine the model in order to obtain a more detailed description of the stress/strain field. To validate this approach, different assessments and numerical results are provided in comparison with solid models. Then, a hierarchical multi-scale approach is proposed for the progressive failure analysis of fiber-reinforced composite structures. In this perspective, two-scales analyses are performed where the macro-scale and micro-scale are taken into account. The first scale, ranging in the global dimension of the model is described as continuum through a a homogenized model. The latter, ranging in the component dimensions (i.e. fibers, matrix portions), the heterogeneity of materials is introduced directly modeling the fiber and matrix phases. At this level, for reducing the computational cost of the analysis, fiber/matrix cells are modelled through the 1D CUF. This second approach is based on the micro-mechanic assumption that in the whole structure a repeating cell of the fiber-reinforced material can be identified, for this reason cells are also addressed as Representative Unit Cells (RUCs) . The information are passed through the scale through a scheme where specific boundary conditions are applied. The multi-scale analysis leads to the prediction of the overall behaviour of the structure from the known material properties of components. Once the stress and strain distributions are given, failure criteria are be taken into account to perform failure analysis. Since the micro-scale is analysed, failure parameters can be calculated directly on components and the different behavior of fiber and matrix materials can be addressed. Integral failure parameters can also be evaluated within the cells or in critical portion of the structure. The hierarchical approach is also used to perform progressive failure analysis introducing the Crack band method in a mesh objective way.
This work is organized as follows: an introduction on the state-of-the-art of composite structures is provided in chapter 1. A brief theoretical introduction to the present 1D Carrera Unified Formulation is given in chapter 2, then the CW approach is described in chapter 3 where numerical examples are provided. In perspective of failure analysis the CW is exploited for the evaluation of integral parameters as shown in chapter 4. Then, the hierarchical two-scale analysis for the progressive failure analysis is introduced in chapter 5 where numerical examples are provided. The failure criteria and the Crack Band method are presented in chapter 6. Main conclusions are drawn in chapter 7.

Contents

Chapter 1

Introduction

The present chapter introduces to the motivations of this work: a brief overview on composite materials and their applications in aerospace is presented in section 1.1; topics and goals are discussed in section 1.2.

1.1 Composite applications in aerospace

The use of composite materials for aerospace applications is greatly advantageous since composites have better specific properties than traditional metallic materials. A composite structure, for instance, could have a ten times higher stiffness and two times lower density than an aluminium made one. Composite material use has proven that strength, corrosion resistance, weight, fatigue life and durability can be significantly improved. Better performances and an efficient reduction in weight are leading to "full composite" design for modern aircraft.
High performance composites (i.e., first boron and then carbon fibers) started being developed in the mid-1960s and early-1970s for military applications. The earliest production usage of high performance composites were on the empennages of the F-14 and F-15 fighter aircraft. Boron/epoxy were used for the horizontal stabilators on both of these aircraft and for the rudders and vertical fins on the F-15. In the mid-1970s, with the maturity of carbon fibers, a carbon/epoxy speedbrake was implemented on the F-15. These first applications resulted in a significant weight saving (about 20%), but they accounted for only a small amounts of the airframe structural weight. The composite usage quickly expanded from only 2% of the airframe on the F-15 to as much as 27% on the AV-8B Harrier by the early-1980s, see Figs. 1.1, [1]. Significant applications included the wing (skins and substructure), the forward fuselage and the horizontal stabilator, all fabricated of carbon/epoxy. Similar trends have been followed for commercial aircraft, although at a slower and more cautious pace.
Nowadays, commercial aircrafts such as the 787 by Boeing as well as the A350 by Airbus are about 50% composite made. Airbus introduced composites primarily for horizontal stabilizers and vertical fins on their A300 series, see Figure 1.2. Recently the A350 XWB has successfully completed its first test flights operating with more than 53% of the overall

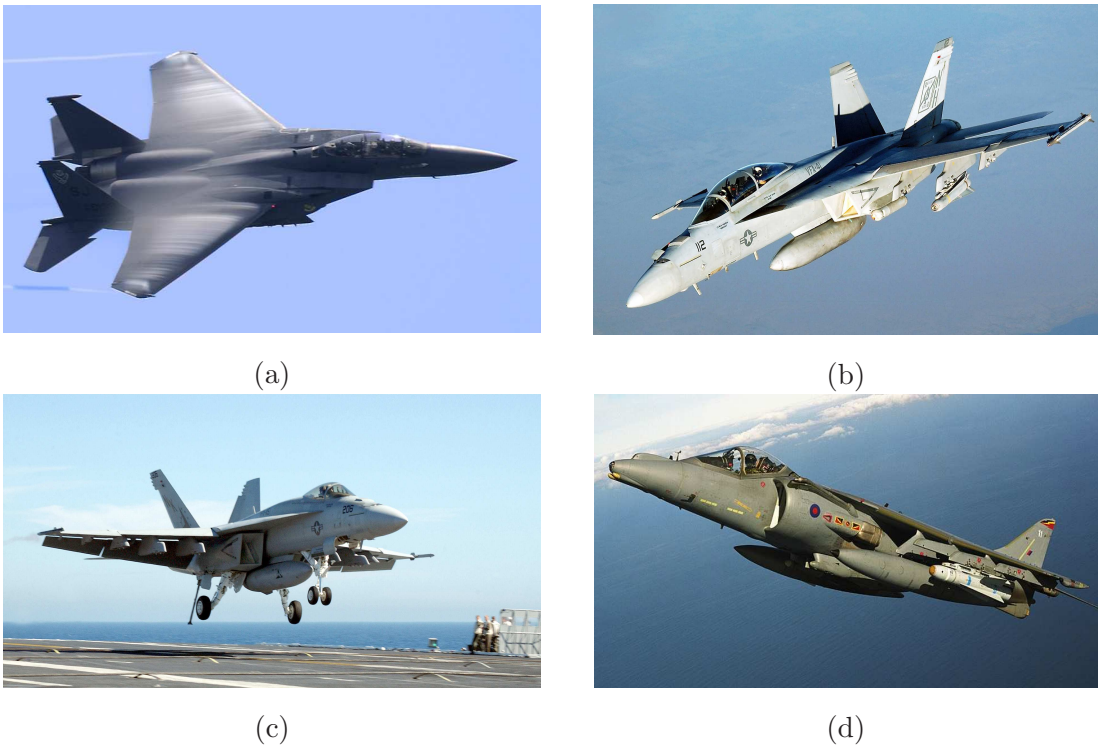

(a) (b)

(c) (d)

Figure 1.1. Utilisation of composite material in military airplanes: (a) F-15 (early 1970s), 2% composites, (b) F/A-18 A/B (mid-1970s), 10% composites, (c) AV-8B Harrier (early 1980s), 27% composites, (d) F/A-18 E/F (mid-1990s), 22% composites.

airframe in composite materials, as reported in Figure 1.5. Figure 1.3 depicts how the use of composite materials has led to a structural weight reduction of aircrafts over the last decades. The first large scale usage of composites in commercial aircraft occurred in 1985 when the Airbus A320 first flew with composite horizontal and vertical stabilizers. Airbus has applied composites in up to 15% of the overall airframe weight for their A320, A330 and A340 family of aircraft. It has to be noted that, while the percentages are lower for commercial aircraft, the part sizes are much larger in respect to military applications. For example, the Boeing 777 horizontal stabilizer has approximately the same surface area as a Boeing 737 wing. Composites represent about a quarter of the A380 structural weight and more than 50% on the A350XWB. Boeing recently made major commitment in composites deciding to use upwards of 50% on its 787 for both wing and fuselage structures as shown in Fig. 1.6. Data refer to the official websites for both Airbus (www.airbus.com) and Boeing (www.boeing.com).

There are different types of composite that are increasingly being used; the most common are particulate, fiber reinforced and laminated materials. This work focuses on fiber reinforced composites where fibers are characterized by a very high length to diameter ratio. Fibers make the structure stiffer and stronger and are bonded together by means of a matrix material. Matrix materials can be polymers, metals, ceramic or carbon. Composite

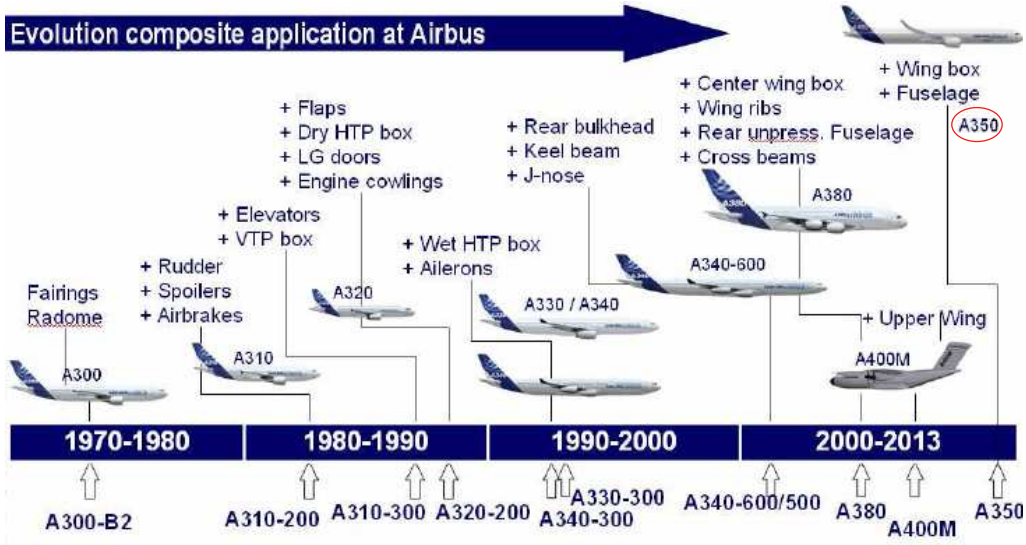

Figure 1.2. Evolution in use of composite structures in Airbus.

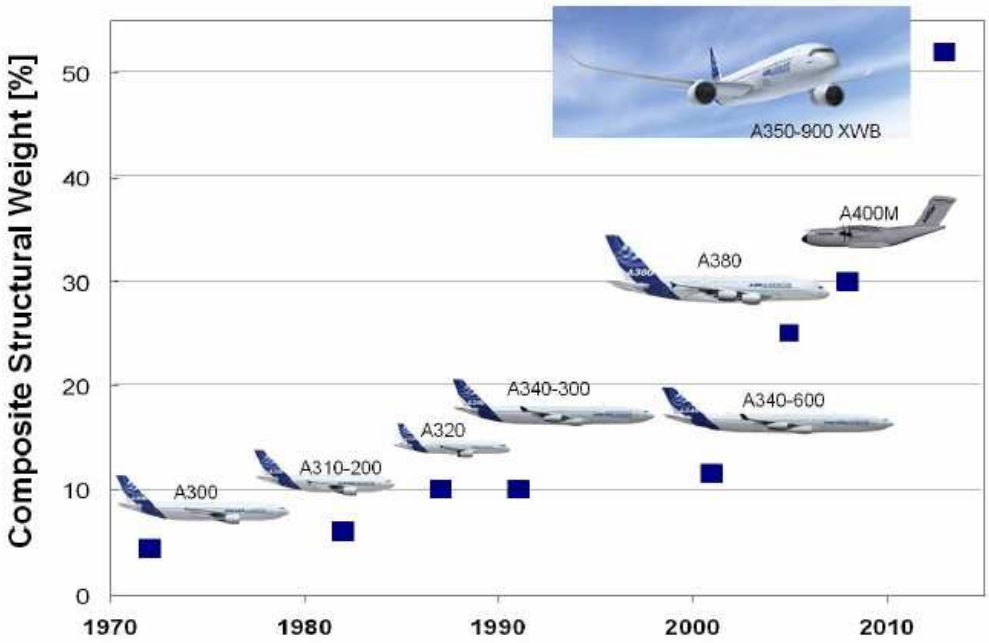

Figure 1.3. Composite structural weight development.

materials display different characteristics and behave differently from metallic materials. A good introduction to the mechanics of composite materials is given by Jones [2]. For certain applications, both macromechanics and micromechanics must be considered for the analysis of composite structures. Micromechanics concerns the analysis of the components

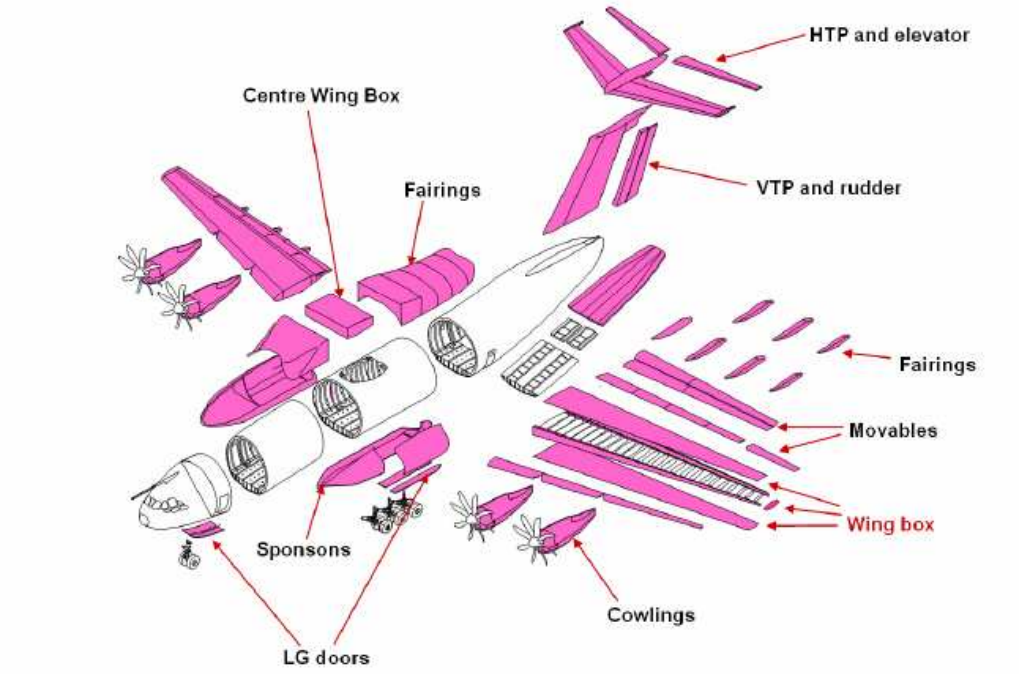

Figure 1.4. Composite Parts in the A400M.

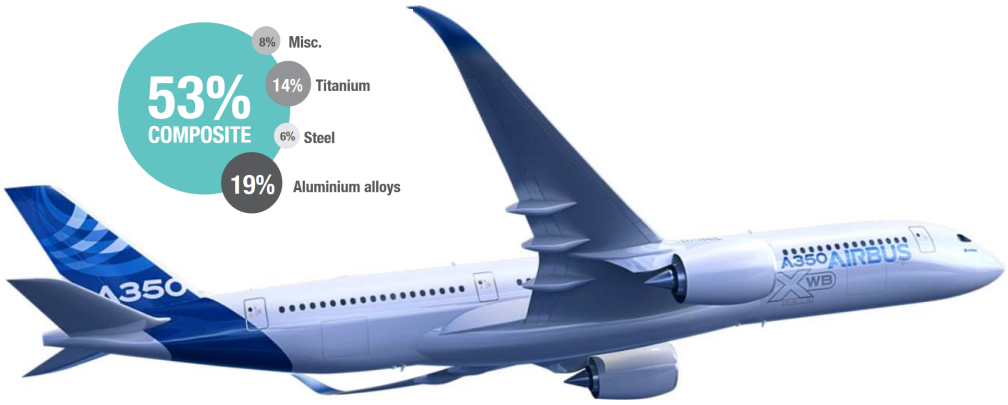

Figure 1.5. Use of composite materials in the A350XWB airframe.

(fibers and matrix) on a microscopic scale. Macromechanics studies the structure from a macroscopic point of view where in which the structure is considered homogeneous.

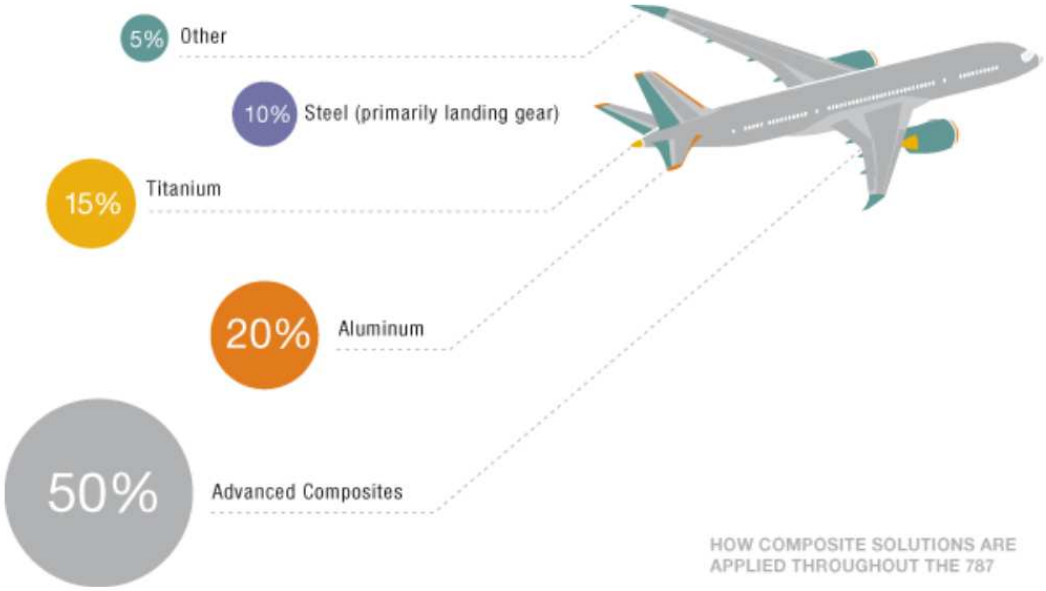

Figure 1.6. Boeing 787 Material Distribution.

1.2 Motivations and Topics of the Thesis

In spite of the advantages previously addressed, there are still many problems that need to be considered when rationalizing the use of composite materials: optimization, scale of production, non-destructive test inspection, fatigue, bolding, etc.. Among these the analysis of the failure mechanisms of layered components is of particular interest. Failure of laminates has, quite a different behaviour than the one of traditional metallic isotropic and homogeneous materials. Composite laminates are non-homogeneous materials with anisotropic behaviour; the failure can initiate at the same time in many different zones and propagate differently. Furthermore each failure mode can influence the other to a considerably degree. Many studies have been conducted on these topics, the most accepted result is that the failure of composites can be seen as a multi-scale phenomenon in which the micro- and macro-scales are involved; both of them have to be considered to determine the failure initiation and propagation. Recent studies have proposed the use of the molecular dynamic analysis at the nano-scale, Representative Volume Elements at the micro-scale and structural elements (solids, beams, plates, shells) at the macro-scale to model the problem. This kind of solution is limited by prohibitive computational costs (hundreds of million of degrees of freedom) and requires the knowledge of the material properties at nano-, micro- and macro-scale. Failure conditions originate as microcracks, as

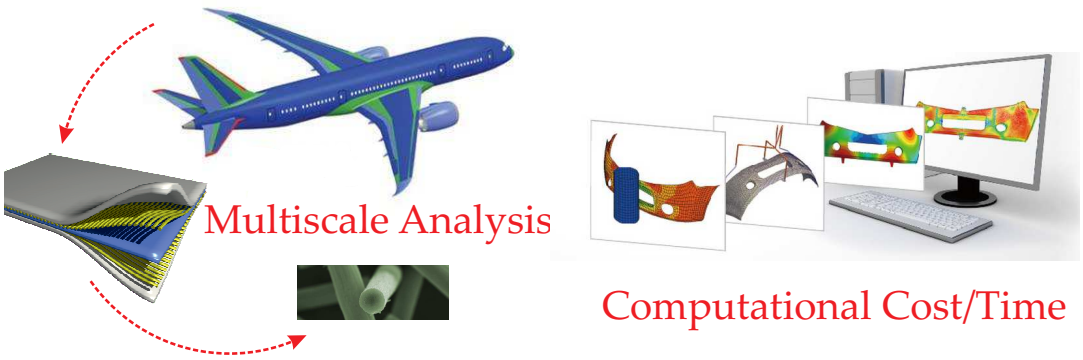

Figure 1.7. Motivations of the present thesis.

fiber breakage and delamination debonding and it depends on the loading configurations. Comprehensive analyses require accurate descriptions at the different scales. However, the accuracy of the model is limited by computational ability; time and cost of the simulations have to be reduced in order to use multiscale approaches. A compromise between accuracy and cost is then required as depicted in Figure 1.7. Many multiscale methods have low reliability and necessitate the introduction of less expensive approaches. The present thesis is focused on the development of a multiscale structural beam model to investigate the failure mechanisms of fiber reinforced composite materials. Beam structures are widely used in many engineering applications. Well known examples in aerospace engineering are aircraft wings and helicopter rotor blades and concrete beams in civil constructions. One-dimensional models are powerful tools for structural analysis due to their simplicity

and low computational cost compared to two- (plate/shell) and three-dimensional (solid) models analyses. The adopted 1D models are derived through Carrera's Unified Formulation (CUF). Advanced displacement-based theories can be exploited since the order of the unknown variables over the cross-section is a free parameter of the formulation. The kinematical field over the beam cross-sections is described by means of Taylor- or Lagrange-like polynomials. Equivalent Single Layer (ESL) and Layer-Wise (LW) description can be used. The main drawbacks of the classical multi-scale models are avoided since:

- the computational costs are very convenient; only few thousands of degrees of freedom (DOF) are used;
- each structural component at any scale level can be modelled by itself. That means that, if a fiber-reinforced laminate is considered, both matrix and fibers can be modelled with 1D elements having their own material properties. This allows:
  1. accounting for non-homogeneities;
  2. using proper failure criteria directly on components;
  3. being able to determine the failure initiation as well as the failure type.

CUF was initially devoted to the development of refined plate and shell theories, see Carrera [3, 4]. Recently, it has been extended to beam modelling in Carrera and Giunta [5] and [6]. The CUF is a hierarchical formulation that considers the order of the theory as an input of the analysis. This particular feature allows dealing with a wide variety of problems with no need of *ad hoc* formulations. Non-classical effects (e.g. warping, in-plane deformations, shear effects, bending-torsion coupling) are accounted for by opportunely increasing the order of the adopted model. Furthermore, since this approach is developed in the finite element framework it is possible to deal with arbitrary geometries, boundary conditions and loadings. Within the CUF, two classes of models are proposed, the Taylor-expansion class (TE) and the Lagrange-expansion class (LE). TE models exploit $N-order$ Taylor-like polynomials to define the displacement field above the cross-section with N as a free parameter of the formulation. Static [7, 8, 9] and free-vibration analyses [10, 11, 12] showed the strength of CUF 1D models in dealing with arbitrary geometries, thin-walled structures and local effects. Moreover, asymptotic-like analyses leading to reduced refined models were carried out [13].
The LE class is based on Lagrange-like polynomials to discretize the cross-section displacement field. LE models have only pure displacement variables. Static analyses on isotropic [14] and composite structures [15] revealed the strength of LE models in dealing with open cross-sections, arbitrary boundary conditions and obtaining Layer-Wise descriptions of the 1D model.

Chapter 2

Structural models

This chapter is devoted to introduce the 1D CUF. The coordinate system and the notation to define the displacement, stress, and strain vectors used in the following chapters have been introduced in section 2.1; the constitutive equations can be found in section 2.2. In the present work, two main hierarchical higher-order models have been exploited on the base of two polynomial classes: the Taylor (TE) and Lagrange (LE) polynomials. The TE and LE formulations are explained in section 2.3. The Finite Element framework is addressed in section 2.4 where the "Foundamental Nuclei" are obtained.

2.1 Coordinate Frame and Preliminaries

Structures which have one or more predominant dimensions compared to the others can be analyzed efficiently using 1D- or 2D-formulations: In the finite element framework, a 1D (beam) element is a structure whose longitudinal length is predominant with respect to the other two orthogonal dimensions; a 2D (plate/shell) element is a flat structure which has two dimensions bigger than the third one, called thickness. The use of 1D- and 2D-elements can be extremely advantageous in many engineering problems. Classical structural theories work well for certain class problems (slender beams, thin plates, etc.) but more sophisticated theories are required to analyze more complex configurations. When compared to 3D results, higher order models can provide accurate results with a reduced computational cost, they can be use to overcome the limitations of classical theories and to perform analysis with a more convenient computational cost. The CUF is a hierarchical formulation which considers the order of the theory as an input of the analysis. This permits us to deal with a wide variety of problems with no need of *ad hoc* formulations. Non-classical effects (e.g. warping, in-plane deformations, shear effects, bending-torsion coupling) are accounted for by opportunely increasing the order of the adopted model. The formulation is implemented within the finite element method to deal with arbitrary geometries, boundary conditions, and loading configurations. The displacement vector is defined as:

$$\mathbf{u}(x,y,z) = \left\{ \begin{array}{ccc} u_x & u_y & u_z \end{array} \right\}^T \tag{2.1}$$

where x, y, and z are orthonormal axes as shown in Figure 2.1. Stress, $\boldsymbol{\sigma}$, and strain, $\boldsymbol{\varepsilon}$,

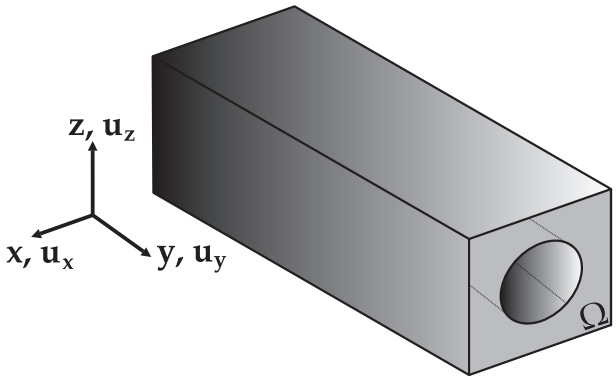

Figure 2.1. Coordinate frame.

components are grouped as follows:

$$\boldsymbol{\sigma} = \left\{ \begin{array}{cccccc} \sigma_{xx} & \sigma_{yy} & \sigma_{zz} & \sigma_{xy} & \sigma_{xz} & \sigma_{yz} \end{array} \right\}^T \tag{2.2}$$

$$\boldsymbol{\varepsilon} = \left\{ \begin{array}{cccccc} \varepsilon_{xx} & \varepsilon_{yy} & \varepsilon_{zz} & 2\varepsilon_{xy} & 2\varepsilon_{xz} & 2\varepsilon_{yz} \end{array} \right\}^T \tag{2.3}$$

where the superscript T represents the transposition operator. Stress and strain components can be split into terms related to the beam axis σ_n, ε_n and the beam cross-section σ_p, ε_p:

$$\boldsymbol{\sigma}_n = \left\{ \begin{array}{ccc} \sigma_{yy} & \sigma_{xy} & \sigma_{yz} \end{array} \right\}^T, \boldsymbol{\varepsilon}_n = \left\{ \begin{array}{ccc} \varepsilon_{yy} & \gamma_{xy} & \gamma_{yz} \end{array} \right\}^T \tag{2.4}$$

$$\boldsymbol{\sigma}_p = \left\{ \begin{array}{ccc} \sigma_{xx} & \sigma_{xz} & \sigma_{zz} \end{array} \right\}^T, \boldsymbol{\varepsilon}_p = \left\{ \begin{array}{ccc} \varepsilon_{xx} & \gamma_{xz} & \varepsilon_{zz} \end{array} \right\}^T \tag{2.5}$$

where the engineering shear strains are introduced:

$$\gamma_{ij} = 2\varepsilon_{ij} \; i \neq j \tag{2.6}$$

Linear strain-displacement relations are used.

$$\boldsymbol{\epsilon} = \boldsymbol{D}\mathbf{u} = (\boldsymbol{D}_y + \boldsymbol{D}_\Omega)\mathbf{u} \tag{2.7}$$

where

$$\boldsymbol{D} = \begin{bmatrix} \frac{\partial}{\partial x} & 0 & 0 \\ 0 & \frac{\partial}{\partial y} & 0 \\ 0 & 0 & \frac{\partial}{\partial z} \\ \frac{\partial}{\partial y} & \frac{\partial}{\partial x} & 0 \\ \frac{\partial}{\partial z} & 0 & \frac{\partial}{\partial x} \\ 0 & \frac{\partial}{\partial z} & \frac{\partial}{\partial y} \end{bmatrix} = \begin{bmatrix} \frac{\partial}{\partial x} & 0 & 0 \\ 0 & 0 & 0 \\ 0 & 0 & \frac{\partial}{\partial z} \\ 0 & \frac{\partial}{\partial x} & 0 \\ \frac{\partial}{\partial z} & 0 & \frac{\partial}{\partial x} \\ 0 & \frac{\partial}{\partial z} & 0 \end{bmatrix} + \begin{bmatrix} 0 & 0 & 0 \\ 0 & \frac{\partial}{\partial y} & 0 \\ 0 & 0 & 0 \\ \frac{\partial}{\partial y} & 0 & 0 \\ 0 & 0 & 0 \\ 0 & 0 & \frac{\partial}{\partial y} \end{bmatrix} = [\boldsymbol{D}_\Omega] + [\boldsymbol{D}_y] \tag{2.8}$$

2.2 Constitutive Equations

If the deformations remain small, linear constitutive laws, known as generalized Hook's law, can be exploited to obtain the stress components.

$$\boldsymbol{\sigma} = \boldsymbol{C}\boldsymbol{\varepsilon} \tag{2.9}$$

According to the notation introduced in 2.1

$$\begin{aligned} \boldsymbol{\sigma_p} = &\quad \boldsymbol{C_{pp}\varepsilon_p} + \boldsymbol{C_{pn}\varepsilon_n} \\ \boldsymbol{\sigma_n} = &\quad \boldsymbol{C_{np}\varepsilon_p} + \boldsymbol{C_{nn}\varepsilon_n} \end{aligned} \tag{2.10}$$

Considering the 3D state of stress $\boldsymbol{C}$ is a 6×6 square matrix where the 36 coefficients may not be all independent from each other and depend on the material constitution.

$$\begin{Bmatrix} \sigma_{33} \\ \sigma_{22} \\ \sigma_{11} \\ \sigma_{23} \\ \sigma_{13} \\ \sigma_{12} \end{Bmatrix} = \begin{bmatrix} C_{33} & C_{32} & C_{31} & C_{34} & C_{35} & C_{36} \\ C_{23} & C_{22} & C_{21} & C_{24} & C_{25} & C_{26} \\ C_{13} & C_{12} & C_{11} & C_{14} & C_{15} & C_{16} \\ C_{43} & C_{42} & C_{41} & C_{44} & C_{45} & C_{46} \\ C_{53} & C_{52} & C_{51} & C_{54} & C_{55} & C_{56} \\ C_{63} & C_{62} & C_{61} & C_{64} & C_{65} & C_{66} \end{bmatrix} \begin{Bmatrix} \varepsilon_{33} \\ \varepsilon_{22} \\ \varepsilon_{11} \\ \varepsilon_{23} \\ \varepsilon_{13} \\ \varepsilon_{12} \end{Bmatrix} \tag{2.11}$$

In particular, when material properties depend on the direction in which they are measured all 36 parameters are independent from each other; if in the material system can be identified any plane of symmetry, the coefficients can be reduced. If orthotropic material are taken into account the material system has three mutually perpendicular planes of symmetry. In this case the coefficients can be reduced to 9 as shown in Equation 2.12 where $C_{23} = C_{32}$, $C_{13} = C_{31}$ and $C_{12} = C_{21}$.

$$\begin{Bmatrix} \sigma_{33} \\ \sigma_{22} \\ \sigma_{11} \\ \sigma_{23} \\ \sigma_{13} \\ \sigma_{12} \end{Bmatrix} = \begin{bmatrix} C_{33} & C_{32} & C_{31} & 0 & 0 & 0 \\ C_{23} & C_{22} & C_{21} & 0 & 0 & 0 \\ C_{13} & C_{12} & C_{11} & 0 & 0 & 0 \\ 0 & 0 & 0 & C_{44} & 0 & 0 \\ 0 & 0 & 0 & 0 & C_{55} & 0 \\ 0 & 0 & 0 & 0 & 0 & C_{66} \end{bmatrix} \begin{Bmatrix} \varepsilon_{33} \\ \varepsilon_{22} \\ \varepsilon_{11} \\ \varepsilon_{23} \\ \varepsilon_{13} \\ \varepsilon_{12} \end{Bmatrix} \tag{2.12}$$

The stiffness coefficient C_{ij} for an orthotropic material expressed in terms of the engineering constants are also reported in [16].

$$\begin{array}{ccc} C_{11} = \frac{E_1(1-\nu_{23}\nu_{32})}{\Delta}; & C_{12} = \frac{E_1(\nu_{21}+\nu_{23}\nu_{31})}{\Delta}; & C_{13} = \frac{E_1(\nu_{31}+\nu_{21}\nu_{32})}{\Delta}; \\ C_{21} = \frac{E_2(\nu_{12}+\nu_{13}\nu_{32})}{\Delta}; & C_{22} = \frac{E_2(1-\nu_{13}\nu_{31})}{\Delta}; & C_{23} = \frac{E_2(\nu_{32}+\nu_{12}\nu_{31})}{\Delta}; \\ C_{31} = \frac{E_3(\nu_{13}+\nu_{12}\nu_{23})}{\Delta}; & C_{32} = \frac{E_3(\nu_{23}+\nu_{13}\nu_{21})}{\Delta}; & C_{33} = \frac{E_3(1-\nu_{12}\nu_{21})}{\Delta}; \\ C_{44} = G_{12} & C_{55} = G_{13} & C_{66} = G_{23} \end{array} \tag{2.13}$$

where E_i denotes Young's moduli in the ith-material direction, ν_{ij} is the Poisson's ratio for transverse strain in the $j-th$ direction when stressed in the $i-th$ direction and

$$\Delta = 1 - \nu_{12}\nu_{21} - \nu_{13}\nu_{32} - \nu_{23}\nu_{32} - \nu_{12}\nu_{23}\nu_{31} - \nu_{13}\nu_{21}\nu_{32} \tag{2.14}$$

If an isotropic material is considered the properties don't change depending on the directions in which they are measured and the C matrix is further reduced. Infinite planes of symmetry can be found and there are just 3 independent coefficients as shown in 2.15

$$\begin{aligned} C_{11} = C_{22} = C_{33} &= \tfrac{(1-\nu)E}{(1+\nu)(1-2\nu)} \\ C_{44} = C_{55} = C_{66} &= \tfrac{E}{2(1+\nu)} \\ C_{13} = C_{12} = C_{23} &= \tfrac{\nu E}{(1+\nu)(1-2\nu)} \end{aligned} \tag{2.15}$$

where E, $G = \frac{E}{2(1+\nu)}$ and $\lambda = \frac{\nu E}{(1+\nu)(1-2\nu)}$ are also called Lamé's coefficients. The C matrix for isotropic material is reported in equation 2.16.

$$\begin{Bmatrix} \sigma_{33} \\ \sigma_{22} \\ \sigma_{11} \\ \sigma_{23} \\ \sigma_{13} \\ \sigma_{12} \end{Bmatrix} = \begin{bmatrix} C_{33} & C_{13} & C_{13} & 0 & 0 & 0 \\ C_{13} & C_{33} & C_{13} & 0 & 0 & 0 \\ C_{13} & C_{13} & C_{33} & 0 & 0 & 0 \\ 0 & 0 & 0 & C_{44} & 0 & 0 \\ 0 & 0 & 0 & 0 & C_{44} & 0 \\ 0 & 0 & 0 & 0 & 0 & C_{44} \end{bmatrix} \begin{Bmatrix} \varepsilon_{33} \\ \varepsilon_{22} \\ \varepsilon_{11} \\ \varepsilon_{23} \\ \varepsilon_{13} \\ \varepsilon_{12} \end{Bmatrix} \tag{2.16}$$

2.2.1 Constitutive equations in the physical coordinate frame

Constitutive relations are written in the principal material coordinate frame, refered as (1,2,3) and shown in Fig. 2.2. For composite laminate, the principal material coordinate frame can be different for each ply depending of the laminate layup. The physical coordinate system is referred to the whole structure while the material system is defined with respect of the fiber directions for each ply. The material system for the laminate in Fig. 2.2 is defined as follow: the 2-axis is going in the fiber longitudinal direction, the 3-axis is aligned with the fiber transversal in-plane direction T (in the plane of the lamina) and the 1-axis is the transversal out-of-plane direction Z. Coordinate transformation equations are employed to obtain the stress vector in physical coordinates (x,y,z). In this case, to convert the stress and strain in the physical frame, the material axes 2 and 3 are rotated by a positive counter clockwise angle θ about the z axis, coincident to axis 1, x- and y-axes of the physical coordinate frame. The current state of stress and strain is then obtained applying the transformation matrix T, to the material system coordinates:

$$\{\sigma\} = [T]\{\sigma\}_m \qquad \{\varepsilon\} = [T]\{\varepsilon\}_m \tag{2.17}$$

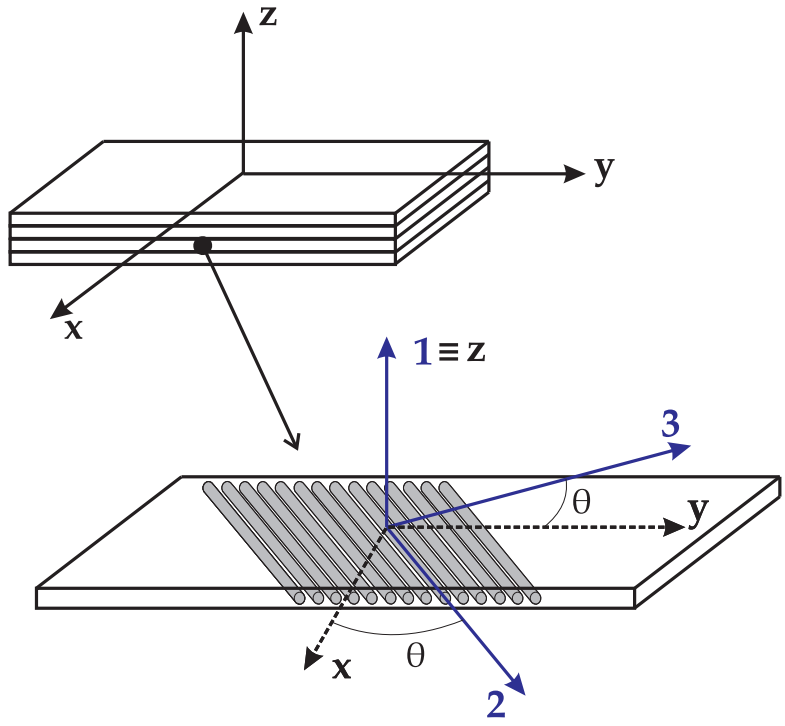

Figure 2.2. Physical (x,y,z) and material (1,2,3) reference systems.

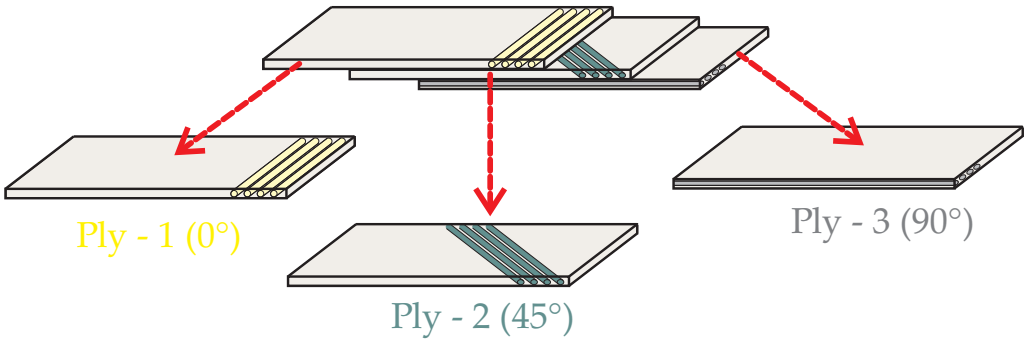

Figure 2.3. Composite layup.

where $[T]$ is reported in 2.18:

$$[T] = \begin{bmatrix} cos^2\theta & sin^2\theta & 0 & 0 & 0 & sin2\theta \\ sin^2\theta & cos^2\theta & 0 & 0 & 0 & -sin2\theta \\ 0 & 0 & 1 & 0 & 0 & 0 \\ 0 & 0 & 0 & \cos\theta & -sin\theta & 0 \\ 0 & 0 & 0 & sin\theta & \cos\theta & 0 \\ -cos\theta sin\theta & sin\theta cos\theta & 0 & 0 & 0 & cos^2\theta - sin^2\theta \end{bmatrix} \tag{2.18}$$

$$\{\sigma\} = [T][C][T]^T \{\varepsilon\} \tag{2.19}$$

$\tilde{C}$ is the transformed material stiffness matrix where the elastic coefficients are referred to the physical coordinate system (x,y,z):

$$\tilde{C} = [T][C][T]^T \tag{2.20}$$

The Hook's law can then be written in the physical coordinate frame as follow 2.21:

$$\begin{Bmatrix} \sigma_{yy} \\ \sigma_{xx} \\ \sigma_{zz} \\ \sigma_{xz} \\ \sigma_{yz} \\ \sigma_{xy} \end{Bmatrix} = \begin{bmatrix} \tilde{C}_{33} & \tilde{C}_{23} & \tilde{C}_{13} & 0 & 0 & \tilde{C}_{36} \\ \tilde{C}_{23} & \tilde{C}_{22} & \tilde{C}_{12} & 0 & 0 & \tilde{C}_{26} \\ \tilde{C}_{13} & \tilde{C}_{12} & \tilde{C}_{11} & 0 & 0 & \tilde{C}_{33} \\ 0 & 0 & 0 & \tilde{C}_{44} & \tilde{C}_{45} & 0 \\ 0 & 0 & 0 & \tilde{C}_{45} & \tilde{C}_{55} & 0 \\ \tilde{C}_{36} & \tilde{C}_{26} & \tilde{C}_{16} & 0 & 0 & \tilde{C}_{66} \end{bmatrix} \begin{Bmatrix} \varepsilon_{yy} \\ \varepsilon_{xx} \\ \varepsilon_{zz} \\ 2\varepsilon_{xz} \\ 2\varepsilon_{yz} \\ 2\varepsilon_{xy} \end{Bmatrix} \tag{2.21}$$

$$\begin{aligned}
\tilde{C}_{33} &= C_{33}cos^4\theta + 2(C_{23} + 2C_{66})sin^2\theta cos^2\theta + C_{22}sin^4\theta \\
\tilde{C}_{23} &= C_{23}(sin^4\theta + cos^4\theta) + (C_{33} + C_{22} + 4C_{66})sin^2\theta cos^2\theta \\
\tilde{C}_{13} &= C_{13}cos^2\theta + C_{12}sin^2\theta \\
\tilde{C}_{36} &= (-C_{33} + C_{23} + 2C_{66})sin\theta cos^3\theta + (C_{22} - C_{23} - 2C_{66})sin^3\theta cos\theta \\
\tilde{C}_{22} &= C_{22}cos^4\theta + 2(C_{23} + 2C_{66}sin^2\theta cos^2\theta + C_{33}sin^4\theta \\
\tilde{C}_{12} &= C_{12}cos^2\theta + C_{13}sin^2\theta \\
\tilde{C}_{26} &= (-C_{33} + C_{23} + 2C_{66})sin^3\theta cos\theta + (C_{22} - C_{23} - 2C_{66})sin\theta cos^3\theta \\
\tilde{C}_{11} &= C_{11} \\
\tilde{C}_{16} &= (C_{12} - C_{13})sin\theta cos\theta \\
\tilde{C}_{44} &= C_{44}cos^2\theta + C_{55}sin^2\theta \\
\tilde{C}_{45} &= (C_{44} - C_{55})sin\theta cos\theta \\
\tilde{C}_{55} &= C_{55}cos^2\theta + C_{44}sin^2\theta \\
\tilde{C}_{66} &= (C_{33} + C_{22} - 2C_{23} - 2C_{66})sin^2\theta cos^2\theta + C_{66}(sin^4\theta + cos^4\theta)
\end{aligned} \tag{2.22}$$

2.3 Hierarchical Higher-Order Models

In the CUF framework, the displacement field can be approximated through the expansion of generic functions, F_τ, as shown in Equation 2.23,

$$\mathbf{u} = F_\tau \mathbf{u}_\tau, \qquad \tau = 1,2,....,M \tag{2.23}$$

where F_τ vary over the cross-section. $\mathbf{u}_\tau$ is the displacement vector and M stands for the number of terms of the expansion. According to the Einstein notation, the repeated subscript, τ, indicates summation. The choice of F_τ determines the adopted class of 1D CUF model.

2.3.1 The Taylor Expansion class (TE)

The Taylor Expansion class (TE) is based on Taylor-like polynomial expansions, $x^i\ z^j$, of the displacement field over the cross-section of the structure (i and j are positive integers). The order N of the expansion is arbitrary and is set as an input of the analysis. A convergence study is usually needed to choose N for a given structural problem. For example, the second-order model, $N = 2$, has the following kinematic model:

$$\begin{aligned} u_x &= u_{x_1} + x\ u_{x_2} + z\ u_{x_3} + x^2\ u_{x_4} + xz\ u_{x_5} + z^2\ u_{x_6} \\ u_y &= u_{y_1} + x\ u_{y_2} + z\ u_{y_3} + x^2\ u_{y_4} + xz\ u_{y_5} + z^2\ u_{y_6} \\ u_z &= u_{z_1} + x\ u_{z_2} + z\ u_{z_3} + x^2\ u_{z_4} + xz\ u_{z_5} + z^2\ u_{z_6} \end{aligned} \tag{2.24}$$

The 1D model described by Eqs. 2.24 has 18 generalized displacement variables; three constant, six linear, and nine parabolic terms. Classical beam theories, Euler-Bernoulli (EBBT) and Timoshenko (TBT), can be obtained as particular cases of the $N = 1$ model, as shown in [7]. Nevertheless the use of Taylor-type expansions has some intrinsic limitations that led to the introduction of different polynomial classes. In particular the use of TE involves that:

1. the introduced variables have a mathematical meaning (derivatives at the beam axes);
2. higher order terms cannot have a local meaning, they can have cross-section properties only;
3. the extension to large rotation formulation could experience difficulties.

2.3.2 The Lagrange Expansion class (LE)

The Lagrange Expansion class (LE) exploits Lagrange polynomials to build 1D refined models that have displacement variables only. This aspect is of particular interest because:

1. each variable has a precise physical meaning (the problem unknowns are only translational displacements);
2. unknown variables can be put in fixed zones (sub-domains) of the cross-section refining the model in certain areas only;
3. geometrical boundary conditions can be applied in sub-domains of the cross-section (and not only to the whole cross-section);
4. geometrical boundary conditions can also be applied along the beam-axis;
5. cross-sections can be divided into further beam sections and easily assembled since the displacements at each boundary are used as problem unknowns;
6. the extension to geometrically non-linear problems appears more suitable than in the case of Taylor-type higher-order theories.

The isoparametric formulation is exploited to deal with arbitrary shaped geometries. Lagrange polynomials are herein used to describe the cross-section displacement field. Three-, L3, four-, L4, and nine-point, L9, polynomials are adopted. This leads to linear, quasi-linear (bilinear), and quadratic displacement field approximations over the beam cross-section. More refined beam models are implemented by introducing further discretiza-

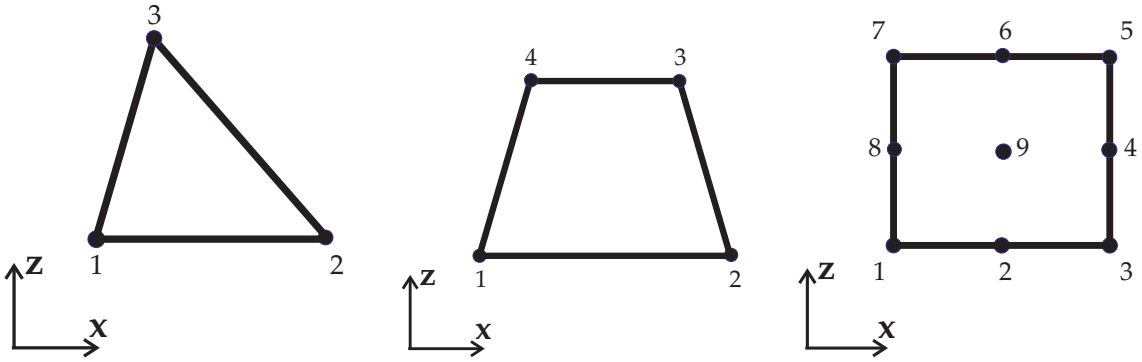

(a) Three-point element, L3. (b) Four-point element, L4. (c) Nine-point element, L9.

Figure 2.4. Cross-Section elements in actual geometry.

tions over the beam cross-section in terms of implemented elements. L3 polynomials are defined on a triangular domain which is identified by three points as shown in Figure 2.5. These points define the element that is used to model the displacement field above the cross-section. The interpolation functions are given by [17]:

$$F_1 = 1 - r - s \qquad F_2 = r \qquad F_3 = s \tag{2.25}$$

Where r and s belong to the triangular domain defined by the points in Table 2.1.

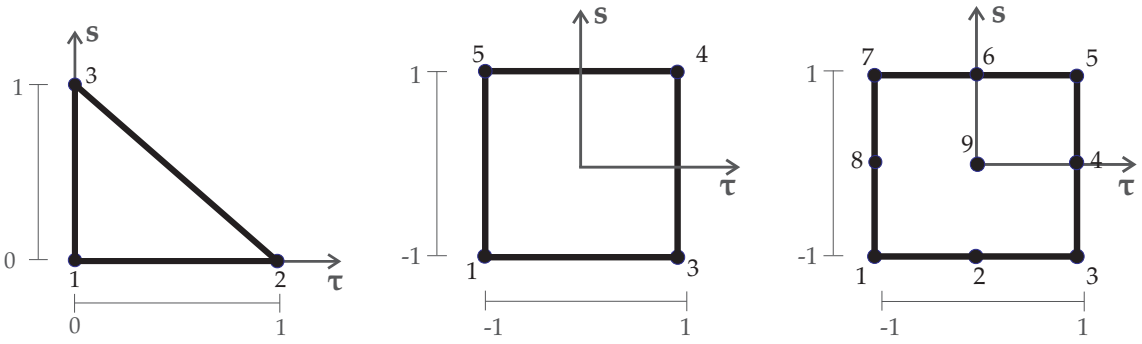

(a) Three-point element, L3. (b) Four-point element, L4. (c) Nine-point element, L9.

Figure 2.5. Cross-Section elements in the natural frames.

Similarly, L4 and L9 cross-section elements are defined on quadrilateral domains. Fig. 2.4b shows the point locations in actual coordinates. The L4 element interpolation functions

Point	r_τ	s_τ
1	0	0
2	1	0
3	0	1

Table 2.1. L3 cross-section element point natural coordinates.

are given by:

$$F_\tau = \frac{1}{4}(1 + r\ r_\tau)(1 + s\ s_\tau) \qquad \tau = 1,2,3,4 \tag{2.26}$$

Where r and s vary from -1 to $+1$. Fig. 2.4b shows the point locations and Table 2.2 reports the point natural coordinates. For the L9 elements the interpolation functions are

Point	r_τ	s_τ
1	-1	-1
2	1	-1
3	1	1
4	-1	1

Table 2.2. L4 cross-section element point natural coordinates.

given by:

$$\begin{aligned} &F_\tau = \tfrac{1}{4}(r^2 + r\ r_\tau)(s^2 + s\ s_\tau) \qquad \tau = 1,3,5,7 \\ &F_\tau = \tfrac{1}{2}s_\tau^2(s^2 - s\ s_\tau)(1 - r^2) + \tfrac{1}{2}r_\tau^2(r^2 - r\ r_\tau)(1 - s^2) \\ &\qquad \tau = 2,4,6,8 \\ &F_\tau = (1 - r^2)(1 - s^2) \qquad \tau = 9 \end{aligned} \tag{2.27}$$

Where r and s from -1 to $+1$. Fig. 2.4c shows the point locations and Table 2.3 reports the point natural coordinates. The displacement field given by an L4 element is:

Point	r_τ	s_τ
1	-1	-1
2	0	-1
3	1	-1
4	1	0
5	1	1
6	0	1
7	-1	1
8	-1	0
9	0	0

Table 2.3. L9 cross-section element point natural coordinates.

$$\begin{aligned} u_x &= F_1\ u_{x_1} + F_2\ u_{x_2} + F_3\ u_{x_3} + F_4\ u_{x_4} \\ u_y &= F_1\ u_{y_1} + F_2\ u_{y_2} + F_3\ u_{y_3} + F_4\ u_{y_4} \\ u_z &= F_1\ u_{z_1} + F_2\ u_{z_2} + F_3\ u_{z_3} + F_4\ u_{z_4} \end{aligned} \tag{2.28}$$

Where u_{x_1},...,u_{z_4} are the displacement variables of the problem and they represent the translational displacement components of each of the four points of the L4 element. The cross-section can be discretized by means of several L-elements. Elements can be assembled through the common nodes to obtain a refined description of the cross-section. Further refinements can be obtained by adding cross-section elements, the beam model will be then defined by the number of cross-section elements used.
It is therefore possible to deal with linear (L3), bilinear (L4), and quadratic (L9) beam theories. The choice of the cross-section discretization (i. e. the choice of the type, the number and the distribution of cross-section elements) is completely independent of the choice of the beam finite element to be used along the beam axis. The L9 interpolation polynomials are given by [17]

$$F_\tau = \tfrac{1}{4}(r^2 + r\ r_\tau)(s^2 + s\ s_\tau) \qquad \tau = 1,3,5,7$$

$$F_\tau = \tfrac{1}{2}s_\tau^2(s^2 - s\ s_\tau)(1 - r^2) + \tfrac{1}{2}r_\tau^2(r^2 - r\ r_\tau)(1 - s^2) \qquad \tau = 2,4,6,8 \tag{2.29}$$

$$F_\tau = (1 - r^2)(1 - s^2) \qquad \tau = 9$$

where r and s range from -1 to $+1$ and r_τ and s_τ are the natural coordinates of the interpolation points over the cross-section. The displacement field given by a L9 element is

$$\begin{aligned} u_x &= F_1\ u_{x_1} + F_2\ u_{x_2} + F_3\ u_{x_3} + F_4\ u_{x_4} + F_5\ u_{x_5} + F_6\ u_{x_6} + F_7\ u_{x_7} + F_8\ u_{x_8} + F_9\ u_{x_9} \\ u_y &= F_1\ u_{y_1} + F_2\ u_{y_2} + F_3\ u_{y_3} + F_4\ u_{y_4} + F_5\ u_{y_5} + F_6\ u_{y_6} + F_7\ u_{y_7} + F_8\ u_{y_8} + F_9\ u_{y_9} \\ u_z &= F_1\ u_{z_1} + F_2\ u_{z_2} + F_3\ u_{z_3} + F_4\ u_{z_4} + F_5\ u_{z_5} + F_6\ u_{z_6} + F_7\ u_{z_7} + F_8\ u_{z_8} + F_9\ u_{z_9} \end{aligned} \tag{2.30}$$

where u_{x_1},...,u_{z_9} are the displacement variables of the problem and they represent the pure displacement components of each of the nine points of the L9 element. This means that LE models provide elements that have only pure displacement variables. L6 models are obtained in the same manner, the explicit expression of these polynomials are not reported here, they can be found in [17].

2.4 FE Formulation and the Fundamental Nucleus

The FE approach is herein adopted to discretize the structure along the y-axis, this process is conducted via a classical finite element methodology based on the Principle of Virtual Displacements. The shape functions, N_i, and the nodal displacement vector, $\mathbf{q}_{\tau i}$, are used and the displacement vector becomes

$$\mathbf{u}(x,y,z) = N_i(y)F_\tau(x,z)\mathbf{q}_{\tau i}, \qquad i = 1,2,....,K \tag{2.31}$$

with

$$\mathbf{q}_{\tau i} = \left\{ \begin{array}{ccc} q_{u_{x_{\tau i}}} & q_{u_{y_{\tau i}}} & q_{u_{z_{\tau i}}} \end{array} \right\}^T \tag{2.32}$$

where K is the number of the nodes on the element. In this work, three different finite element are taken into account that respectively provide a linear, quadratic and cubic approximations along the beam axis. Elements with 2 nodes are denoted as B2 while elements with 3 and 4 nodes are referred respectively as B3 and B4. In Figure 2.6 beam elements are depicted in their natural coordinate frames, node coordinates are also shown for each case. Shape functions are Lagrange polynomials which value is 1 on the i^{th} node and 0 on all the others. The shape functions, N_i, for B2 elements are shown in Equation 2.33 where the coefficients r_i are reported in Table 2.4.

$$\begin{aligned} N_1 &= r_i(r-1) \\ N_2 &= r_i(r+1) \end{aligned} \tag{2.33}$$

Equation 2.34 and 2.35 report respectively shape functions for B3 and B4 elements while

Point	r_i
1	$-1/2$
2	$1/2$

Table 2.4. Shape function coefficients for B2 elements.

the r_i values are listed in Tables 2.5,2.6.

$$\begin{aligned} N_1 &= r_i r(r-1) \\ N_2 &= r_i r(r+1) \\ N_3 &= r_i r(r+1)(r-1) \end{aligned} \tag{2.34}$$

Point	r_i
1	$1/2$
2	$1/2$
3	-1

Table 2.5. Shape function coefficients for B3 elements.

$$\begin{aligned} N_1 &= r_i(r+\tfrac{1}{3})(r-\tfrac{1}{3})(r-1) \\ N_2 &= r_i(r+\tfrac{1}{3})(r-\tfrac{1}{3})(r+1) \\ N_3 &= r_i(r-\tfrac{1}{3})(r+1)(r-1) \\ N_4 &= r_i(r+\tfrac{1}{3})(r+1)(r-1) \end{aligned} \tag{2.35}$$

It can be noted that B2 shape functions are first order Lagrange Polynomials while B3 and B4 respectively second and third orders. Shape functions for these elements can be also found in [18].

Point	r_i
1	$-9/16$
2	$9/16$
3	$27/16$
4	$-27/16$

Table 2.6. Shape function coefficients for B4 elements.

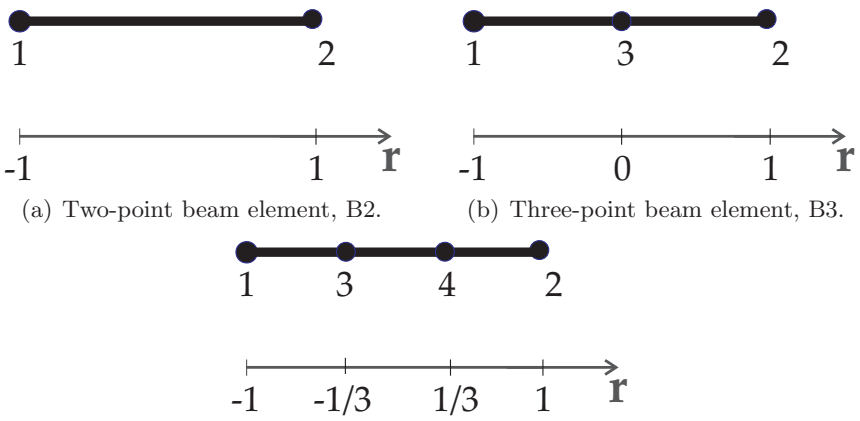

(a) Two-point beam element, B2.

(b) Three-point beam element, B3.

(c) Four-point beam element, B4.

Figure 2.6. Beam-axis shape functions.

The stiffness matrix is obtained via the Principle of Virtual Displacements,

$$\delta L_{int} = \delta L_{ext} \tag{2.36}$$

L_{int} stands for the internal work and L_{ext} is the work of the external loadings. δ stands for the virtual variation. The virtual variation of the internal work is given by

$$\begin{aligned} \delta L_{int} &= \int_V (\delta \boldsymbol{\epsilon}^T \boldsymbol{\sigma}) dV = \\ &= \int_V \delta \mathbf{q}_{\tau i}^T \Big[\boldsymbol{D}^T \Big(N_i(y) F_\tau(x,z) \boldsymbol{I} \Big) \Big] \boldsymbol{C} \Big[\boldsymbol{D} \Big(N_j(y) F_s(x,z) \boldsymbol{I} \Big) \Big] \mathbf{q}_{sj} dV \end{aligned} \tag{2.37}$$

where V is the beam volume. By introducing Eq.2.7 in Eq.2.37, it is possible to rewrite the virtual variation of L_{int} as

$$\begin{aligned}
\delta L_{int} = \delta \mathbf{q}_{\tau i}^T \Bigg\{ \int_V \Big[\Big(\boldsymbol{D}_\Omega + \boldsymbol{D}_y \Big)^T \Big(F_\tau(x,z) N_i(y) \boldsymbol{I} \Big) \Big] \boldsymbol{C} \Big[\Big(\boldsymbol{D}_\Omega + \boldsymbol{D}_y \Big) \Big(N_j(y) F_s(x,z) \boldsymbol{I} \Big) \Big] dV \Bigg\} \mathbf{q}_{sj} = \\
= \delta \mathbf{q}_{\tau i}^T \Bigg\{ \int_l \Big(N_i(y) \Big(\int_\Omega \Big[\boldsymbol{D}_\Omega^T \Big(F_\tau(x,z) \boldsymbol{I} \Big) \Big] \boldsymbol{C} \Big[\boldsymbol{D}_\Omega \Big(F_s(x,z) \boldsymbol{I} \Big) \Big] d\Omega \Big) N_j(y) \Big) dy + \\
+ \int_l \Big(N_i(y) \Big(\int_\Omega \Big[\boldsymbol{D}_\Omega^T \Big(F_\tau(x,z) \boldsymbol{I} \Big) \Big] \boldsymbol{C} F_s(x,z) d\Omega \Big) \boldsymbol{D}_y \Big(N_j(y) \boldsymbol{I} \Big) \Big) dy + \\
+ \int_l \Big(\boldsymbol{D}_y^T \Big(N_i(y) \boldsymbol{I} \Big) \Big(\int_\Omega F_\tau(x,z) \boldsymbol{C} \Big[\boldsymbol{D}_\Omega \Big(F_s(x,z) \boldsymbol{I} \Big) \Big] d\Omega \Big) N_j(y) \Big) dy + \\
+ \int_l \Big(\boldsymbol{D}_y^T \Big(N_i(y) \boldsymbol{I} \Big) \Big(\int_\Omega F_\tau(x,z) \boldsymbol{C} F_s(x,z) d\Omega \Big) \boldsymbol{D}_y \Big(N_j(y) \boldsymbol{I} \Big) \Big) dy \Bigg\} \mathbf{q}_{sj}
\end{aligned} \tag{2.38}$$

where Ω is the cross-section domain and $\mathbf{I}$ is the unit matrix. The variation of the internal work is then written by means of the CUF fundamental nucleus,

$$\delta L_{int} = \delta \mathbf{q}_{\tau i}^T \mathbf{K}^{ij\tau s} \mathbf{q}_{sj} \tag{2.39}$$

$\mathbf{K}^{ij\tau s}$ is the stiffness matrix in the form of the fundamental nucleus. The explicit forms of the 9 components of $\mathbf{K}^{ij\tau s}$ are reported in Equation 2.42.
No assumptions on the approximation order have been done to obtain the fundamental nucleus. It is therefore possible to obtain refined 1D models without changing the formal expression of the nucleus components. This is the key-point of CUF which permits, with only nine FORTRAN statements, to implement any-order one-dimensional theories.
The work of the external forces, δL_{ext}, can be expressed as

$$\begin{aligned}
\delta L_{ext} &= \int_V \delta \boldsymbol{u}^T \tilde{\boldsymbol{F}} dV = \\
&= \delta \mathbf{q}_{\tau i}^T \int_V N_i(y) F_\tau(x,z) \tilde{\boldsymbol{F}} dV \\
&= \delta \mathbf{q}_{\tau i}^T \mathbf{P}^{\tau i}
\end{aligned} \tag{2.40}$$

where $\tilde{\boldsymbol{F}}$ is the generic load and $\mathbf{P}^{\tau i}$ is the vector of the nodal forces.
The global stiffness loading and the unknowns arrays are indicated as $\tilde{\mathbf{K}}$, $\tilde{\mathbf{F}}$ and $\mathbf{q}$, respectively. The following linear algebraic system has to be solved:

$$\tilde{\mathbf{K}} \mathbf{q} = \tilde{\mathbf{P}} \tag{2.41}$$

$$
\begin{aligned}
K_{xx}^{ij\tau s} &= \tilde{C}_{22}\int_\Omega F_{\tau,x}F_{s,x}d\Omega\int_l N_iN_jdy+\tilde{C}_{66}\int_\Omega F_{\tau,z}F_{s,z}d\Omega\int_l N_iN_jdy+\\
&\quad \tilde{C}_{44}\int_\Omega F_\tau F_s d\Omega\int_l N_{i,y}N_{j,y}dy\\
K_{xy}^{ij\tau s} &= \tilde{C}_{23}\int_\Omega F_{\tau,x}F_s d\Omega\int_l N_iN_{j,y}dy+\tilde{C}_{44}\int_\Omega F_\tau F_{s,x}d\Omega\int_l N_{i,y}N_jdy\\
K_{xz}^{ij\tau s} &= \tilde{C}_{12}\int_\Omega F_{\tau,x}F_{s,z}d\Omega\int_l N_iN_jdy+\tilde{C}_{66}\int_\Omega F_{\tau,z}F_{s,x}d\Omega\int_l N_iN_jdy\\
K_{yx}^{ij\tau s} &= \tilde{C}_{44}\int_\Omega F_{\tau,x}F_s d\Omega\int_l N_iN_{j,y}dy+\tilde{C}_{23}\int_\Omega F_\tau F_{s,x}d\Omega\int_l N_{i,y}N_jdy\\
K_{yy}^{ij\tau s} &= \tilde{C}_{55}\int_\Omega F_{\tau,z}F_{s,z}d\Omega\int_l N_iN_jdy+\tilde{C}_{44}\int_\Omega F_{\tau,x}F_{s,x}d\Omega\int_l N_iN_jdy+\\
&\quad \tilde{C}_{33}\int_\Omega F_\tau F_s d\Omega\int_l N_{i,y}N_{j,y}dy\\
K_{yz}^{ij\tau s} &= \tilde{C}_{55}\int_\Omega F_{\tau,z}F_s d\Omega\int_l N_iN_{j,y}dy+\tilde{C}_{13}\int_\Omega F_\tau F_{s,z}d\Omega\int_l N_{i,y}N_jdy\\
K_{zx}^{ij\tau s} &= \tilde{C}_{12}\int_\Omega F_{\tau,z}F_{s,x}d\Omega\int_l N_iN_jdy+\tilde{C}_{66}\int_\Omega F_{\tau,x}F_{s,z}d\Omega\int_l N_iN_jdy\\
K_{zy}^{ij\tau s} &= \tilde{C}_{13}\int_\Omega F_{\tau,z}F_s d\Omega\int_l N_iN_{j,y}dy+\tilde{C}_{55}\int_\Omega F_\tau F_{s,z}d\Omega\int_l N_{i,y}N_jdy\\
K_{zz}^{ij\tau s} &= \tilde{C}_{11}\int_\Omega F_{\tau,z}F_{s,z}d\Omega\int_l N_iN_jdy+\tilde{C}_{66}\int_\Omega F_{\tau,x}F_{s,x}d\Omega\int_l N_iN_jdy+\\
&\quad \tilde{C}_{55}\int_\Omega F_\tau F_s d\Omega\int_l N_{i,y}N_{j,y}dy
\end{aligned}
\tag{2.42}
$$

In multiscale analyses, both TE and LE can be used to model the structure up to the component dimensions. For composite materials, structures have non homogeneous cross-sections. Figure 2.7 and 2.8 provide a graphic explanation of the procedure to assembly the stiffness matrix for a multicomponent structure for both the TE and the LE approaches.

It is necessary to observe that TE lead to a Equivalent Single Layer (ESL) description while through the LE a Layer-Wise formulation is obtained. In this sense, TE operate a sort of homogenization of the fiber and matrix properties. Also, for TE, the number of unknown variables is given by the order of the adopted 1D model; if LE are used, the number of variables depends on the number of L-elements on the cross-section and on their order. To better explain the assembly technique, a simple example for both Tailor and Lagrange polynomial classes is herein given. A generic cross section is described through TE formulation, order of expansion N = 2, while, for the LE, 1 L4 element is used to model the cross-section. 2 B3 elements are used in the y-direction to discretize the y-axis in both cases. In Figure 2.9 the assembly technique for the TE case is shown while in Figure 2.10

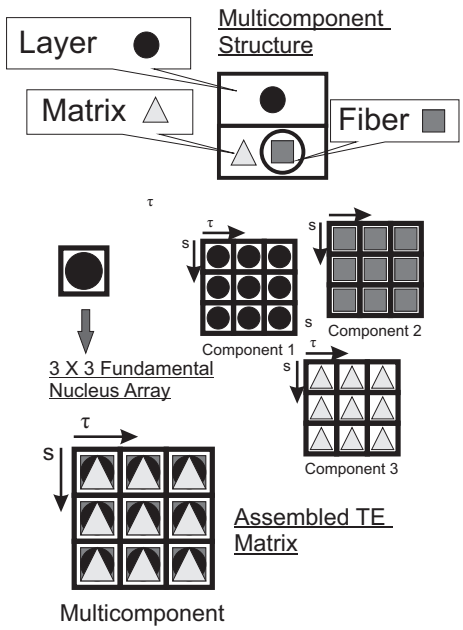

Figure 2.7. TE assembly technique for a multicomponent structure.

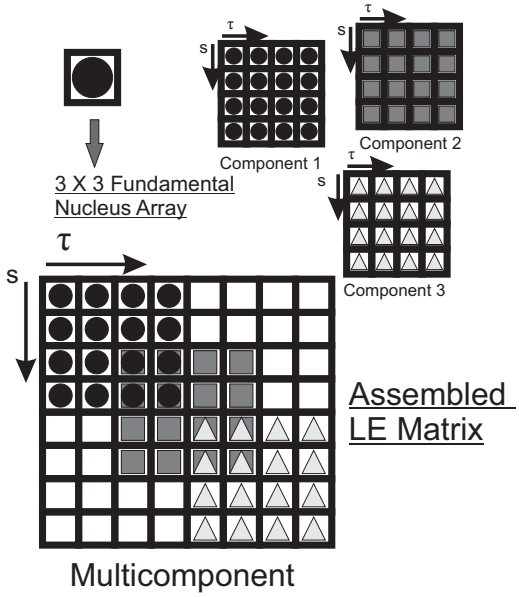

Figure 2.8. LE assembly technique for a multicomponent structure.

the stiffness matrix is obtained for the LE case study. The total stiffness matrix is shown in Figure 2.11, where the square block related to the first and the second beam elements are respectively the 1 B3 stiffness matrices shown in Figures 2.9 and 2.10. For a generic case study the resultant global stiffness matrix is depicted in Figure 2.12. The liner

system in Equation 2.41 is solved in FORTRAN environment though a numerical method. A Gauss elimination algorithm is employed.The stiffness matrix K is rewritten in terms of a lower and upper triangular matrices, L and L^T and a diagonal matrix D through the LDL^T factorization.

$$K = LDL^T \tag{2.43}$$

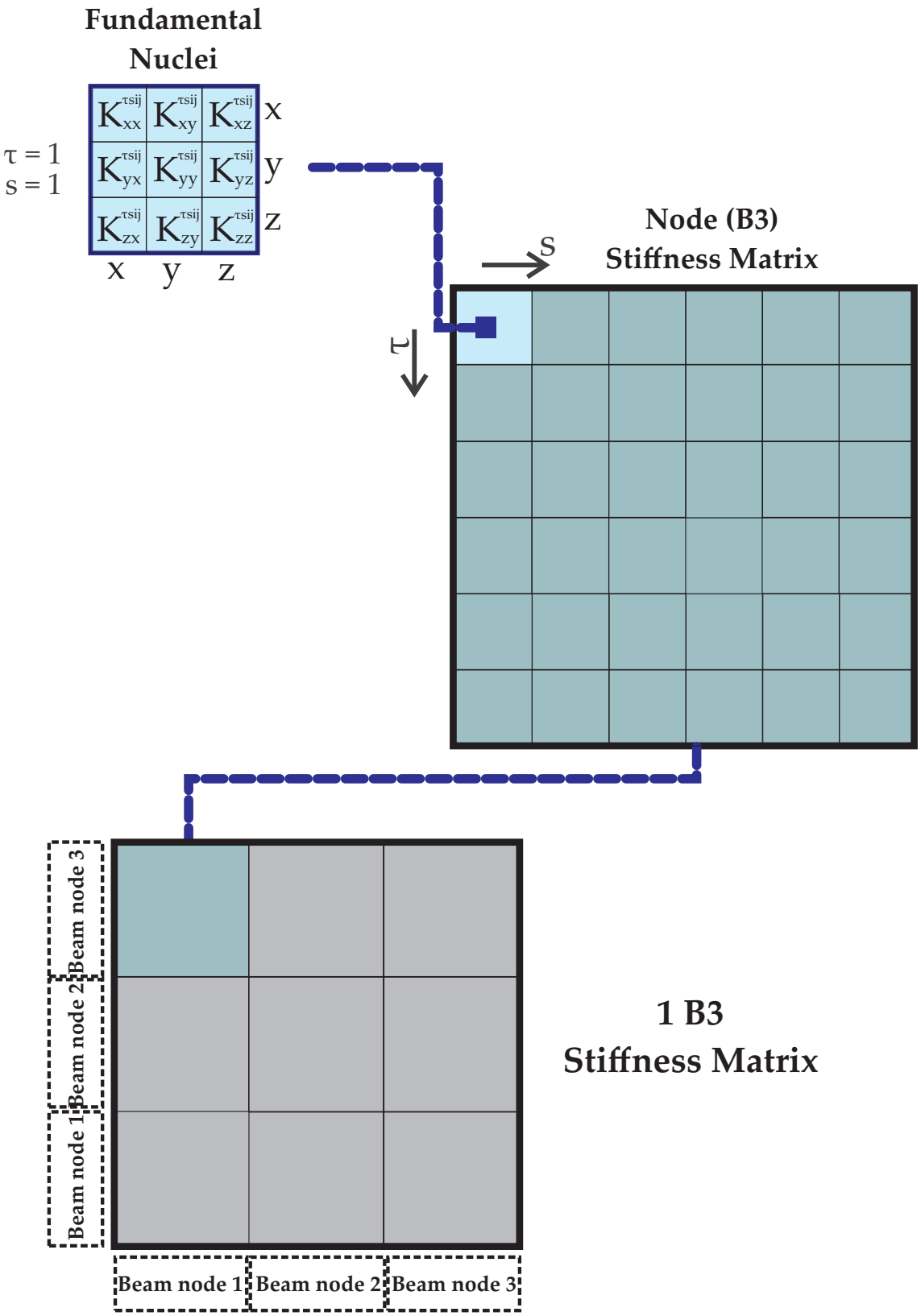

Figure 2.9. Assembly technique for a TE case study, N=2.

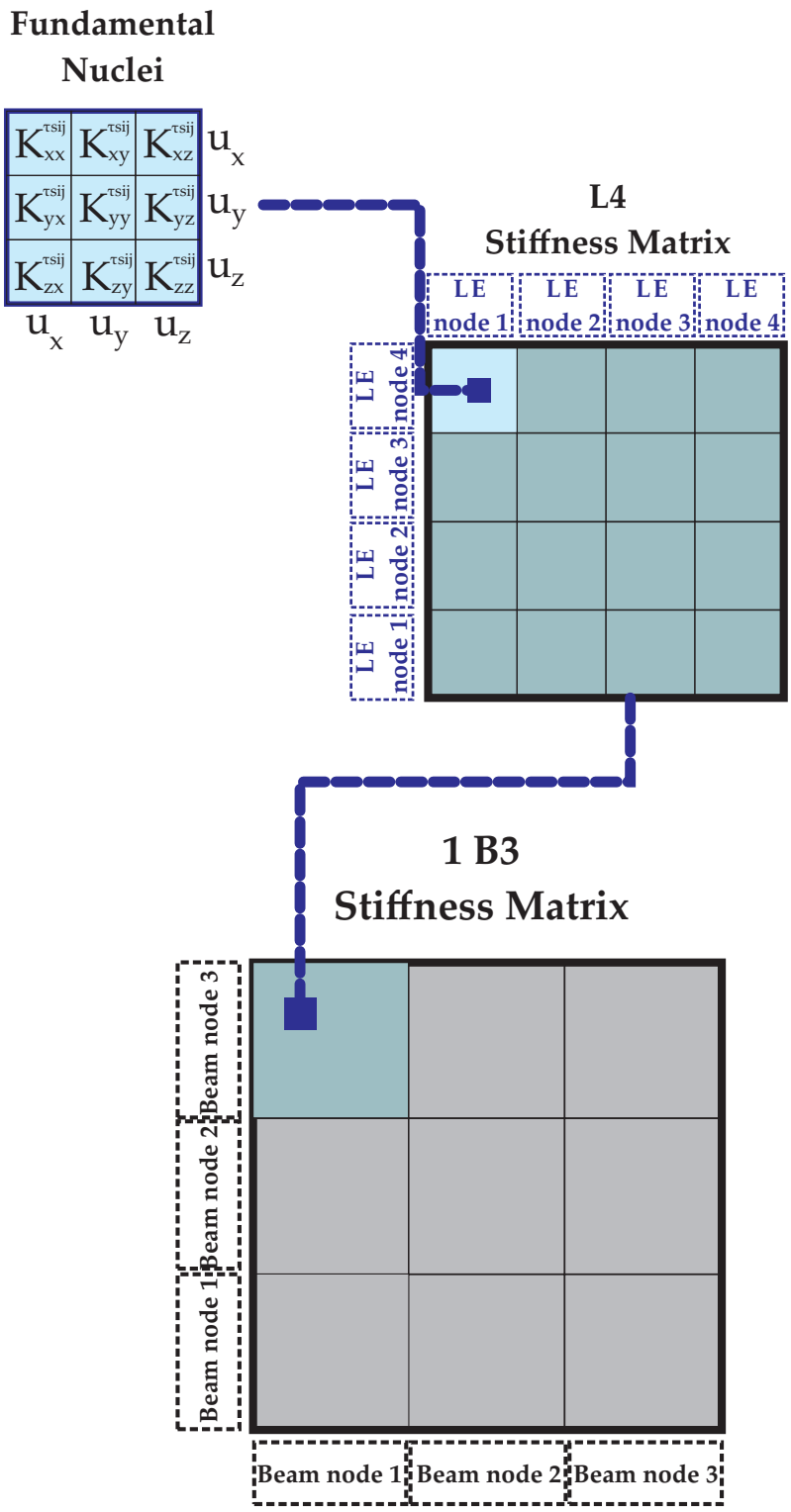

Figure 2.10. Assembly technique for a LE case study, 1 L4 element.

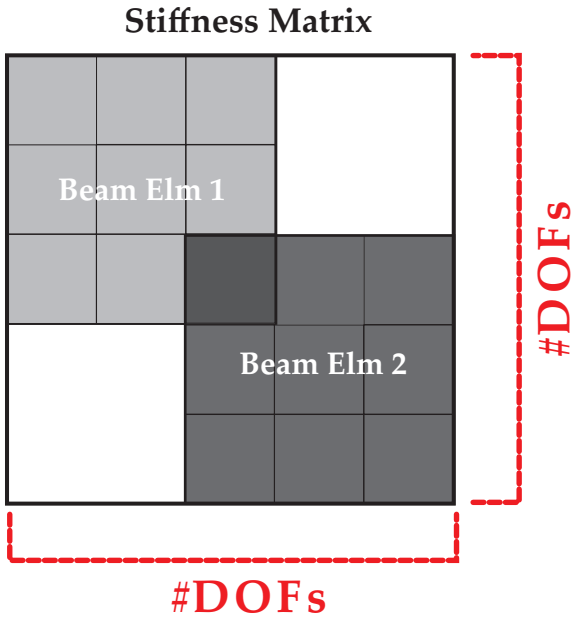

Figure 2.11. Global stiffness matrix for the TE, LE case studies with 1 B3 element in the y-direction.

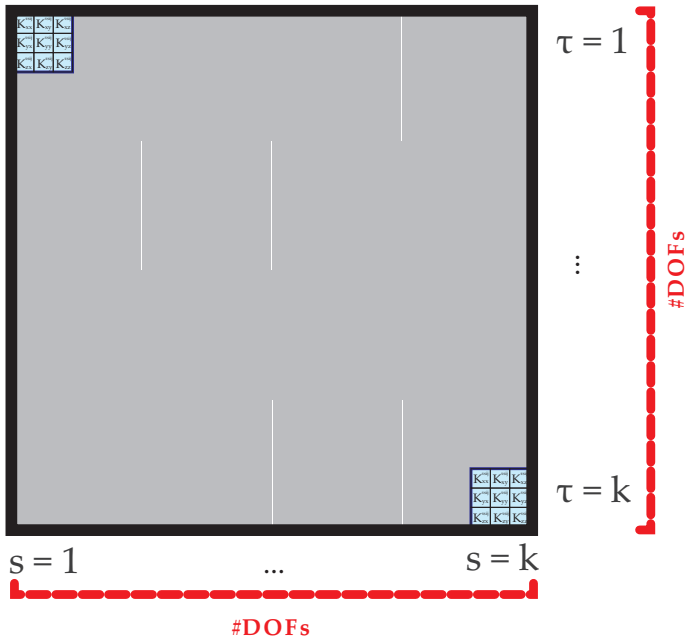

Figure 2.12. K, stiffness matrix obtained through the 1D CUF.

Chapter 3

The Component-Wise Approach

In this chapter the Component-Wise Approach (CW) is introduced. The 1D-CUF Lagrange formulation, described in chapter 2, is exploited in a multiscale perspective for the analysis of fiber-reinforced composite structures. This method has been designed to perform composite failure analysis since it allows a more detailed description of the stress/strain field in certain regions of the model. Preliminary assessments with solid model results are made and numerical examples are carried out on different configurations.

3.1 Introduction

The use of composite materials for aerospace applications is greatly advantageous since composites have better specific properties than traditional metallic materials. A composite structure, for instance, can be some ten times stiffer and two times lighter than an aluminium one. This is the main reason leading to the design of 'full composite' structures for the most advanced aerospace vehicles. In spite of that, there are still many key-problems which have to be considered for a more rational use of composite materials such as fatigue and the characterization of failure mechanisms. A better understanding of these key-problems in composite structure applications demands for enhanced analysis capabilities in various fields. Among these, the present work proposes enhanced structural capabilities to detect accurate stress/strain fields in the matrix, fibers, layers and interfaces of composite layered structures with convenient computational costs.
Many techniques are available to compute accurate stress/strain fields in the different components of a laminated structure (i.e. fibers, matrices and layers), these techniques are briefly discussed hereafter. The natural manner of refining the analysis of 1D and 2D components consists of using 3D solid finite elements. These elements might be employed to discretize single components (fibers and matrices) or to directly model the layer of a laminated structure, that is, fibers and matrices can be modeled as being independent elements or they can be homogenized to compute layer properties. Due to the limitations on the aspect ratio of 3D elements and to the high number of layers used in real applications, computational costs of a solid model could be prohibitive.

Classical theories which are known for traditional beam (1D) and plate/shell (2D) structures had been improved for their application to laminates. Many contributions are known based on higher-order models [19, 20], Zig-zag theories [21, 22, 23, 24] and Layer-Wise (LW) approaches [25, 26, 15]. So-called *global-local* approaches had also been developed by exploiting the superposition of Equivalent Single Layer models (ESL) and LW [27], or by using the Arlequin method to combine higher- and lower-order theories [28, 29, 30].
Many studies on multiscale problems in composites have recently been conducted as in [31]; one of the most important result is that "processes that occur at a certain scale govern the behavior of the system across several (usually larger) scales" [32]. This result implies that the development of analysis capabilities involving many scale levels is necessary in order to properly understand multi-scale phenomena in composites. Various spatial and temporal multiscale methods for composite structures have recently been described by Fish [33] including concurrent and information-passing schemes, block cycles and temporal homogenization approaches. Another excellent overview on multiscale simulations was made by Lu and Kaxiras [32] while an exhaustive description of a new bottom-up multiscale modeling strategy for fiber-reinforced structural composites has been carried out in [34] where virtual test simulations are carried out through the transfer of information between three different length scales defined by the fiber diameter, the ply and laminate thickness. Other recent studies [35, 33, 32] have proposed the use of the molecular dynamic analysis at the nano-scale level, Representative Volume Elements (RVE) at micro-scale and structural elements (e.g. solids, beams, plates or shells) at macro-scale. Various multiscale linear and non-linear techniques can be found in literature for different loading configurations and focused on the prediction of failure processes [36, 37]. Multiscale approaches were exploited to examine the failure of fiber-reinforced laminates subjected to static loading conditions in [38]. The 'Generalized Method of Cell' (GMC) developed by Paley and Aboudi [39, 40, 41] considers fiber and matrix subcells as periodic repeating unit cells or Representative Volume Elements. GMC was used by Pineda and Waas for the multiscale failure analysis of laminated composite panels subjected to blast loads [42] and for the progressive damage and failure modeling of notched laminated fiber reinforced composites [43]. An accurate GMC description can be found in [44]. Two- and three-scale domain decompositions were used by Allix et al. [45] for the delamination analysis. A laminated composite structure was divided in two meso-constituents, substructures and interfaces, whose behavior was derived from the homogenization of micromodels. A two-level domain decomposition method was proposed by Ladeveze et al.[46] as a computational strategy for the analysis of structures described up to the micro-level. In this approach, the unknowns are split in a set of macroscopic quantities, related to the macro-scale, and a set of additive quantities related to the micro-scale. The LATIN method was used as iterative strategy. This approach was tested on fiber-reinforced composite and honeycombs under the assumption of plane strains. Some applications on the damage micro-model of fiber-reinforced laminated composites were reported in [47, 48].
Critical issues of many multiscale approaches proposed in literature are related to the high computational costs (in some cases hundreds of million of degrees of freedom) and the need of material properties at nano-, micro- and macro-scale. These aspects can affect the reliability and applicability of these approaches.

The method proposed in this work is referred to as *Component-wise* and it is based on higher-order 1D models. 'Component-wise' means that each typical component of a composite structures (i.e. layers, fibers and matrices) can be separately modeled by means of a unique formulation. Moreover, in a given model, different scale components can be used simultaneously, that is, homogenized laminates or laminae can be interfaced with fibers and matrices. This permits us to tune the model capabilities by (1) choosing in which portion of the structure a more detailed model has to be used; (2) setting the order of the structural model to be used. A graphic description of the present model capabilities is provided in Figure 3.2 where different components (layers, fibers and matrices) are assembled. In particular, a four layers laminate is modeled including all the components in the third ply and one fiber/matrix cell in the fourth ply, while the first two layers are modelled as single plies. Such a model could be seen as a 'global-local' model since it can be used either to create a *global* model by considering the full laminate or to obtain a *local* model to detect accurate strain/stress distributions in those parts of the structure which could be most likely affected by failure. In other words, the present modeling approach permits us to obtain progressively refined models up to the fiber and matrix dimensions.

3.2 A Component-Wise Approach in the 1D CUF Framework

As intruduced in chapter 1, since composites are increasingly being used in many engineering fields, understanding their failure mechanism has a prominent role in enhancing component designs but requires an accurate description of the mechanical behavior at different levels. Indeed, many micromechanical effects have to be taken into account to evaluate the different possible failure modes. Among many available techniques for the structural analysis of composite structures, multiscale approaches are able to provide a refined description of the stress and strain within the constituent phases. Nevertheless, despite the increasing development in computer hardware, the computational effort of these methods is still prohibitive for extensive applications. The reduction of the computational time and cost required to perform failure analysis has still a prominent role in extending multiscale techniques to large-scale applications.
The aim of the *Component-Wise approach* is to allow us to model each typical component of a composite structure through the 1D CUF formulation. In a finite element framework, for instance, this means that layers, fibers and matrices are modeled by means of the same 1D finite element and, therefore, do not need specific formulations for each component. In other words, the same $\mathbf{K}^{ij\tau s}$ is used for each component. Therefore, fibers and related matrix portions, entire layers and whole multilayers can be modeled at same time. Component can be included in different locations of the structure. As introduced in chapter 2, within the 1D CUF both Taylor- and Lagrange-type polynomials can be used to interpolate the displacement field over the element cross-section. Nevertheless, LE polynomial classes provide a number of benefits that have led to prefer this expansion type to the TE in the developing of the CW approach. In fact, through the 1D LE based based beam formulation the stress and strain fields can be provided with solid-like accuracy with a

significant reduction of DOFs involved. In this chapter CW results are compared to those obtained through the TE-polynomial classes and solid models. Figure 3.1 provides a description of a possible modeling approach. A five layer plate is illustrated and, in the

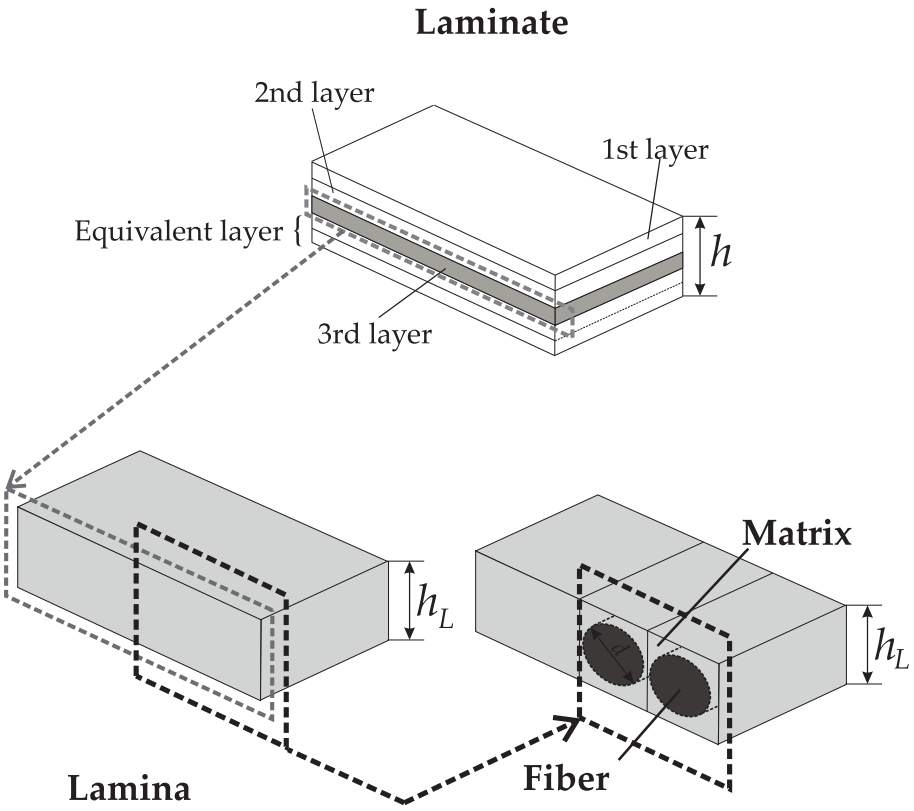

Figure 3.1. Component-Wise approach to simultaneously model layers, fibers and matrices.

top-bottom order, the components are the following: the first two layers, two fiber/matrix cells of the third layer and an equivalent layer of the 4th and 5th lamina. Each component has its own geometrical and material characteristics. In this example, 3 different scales are modeled at the same time, d, the component dimension at micro-scale, h_L, the ply dimension, at meso-scale, and h the whole laminate dimension, at the macro-scale. Single fiber/matrix cell, or RUC (Repeated Unit Cell), refers as a single fiber embedded in a matrix.

Numerical examples were carried out on three different structural models. A single fiber/matrix cell is considered the simplest assessment for the analysis. Cells can be modeled with different geometries and can be combined to build more complex cell configurations to include in any position of the considered model. A double fiber/matrix cell assessment is hereafter proposed. This approach allow to refine the model just in determinate areas keeping the model light and, at the same time, obtaining an accurate description of the stress and strain fields where necessary. Then, multilayered plates are

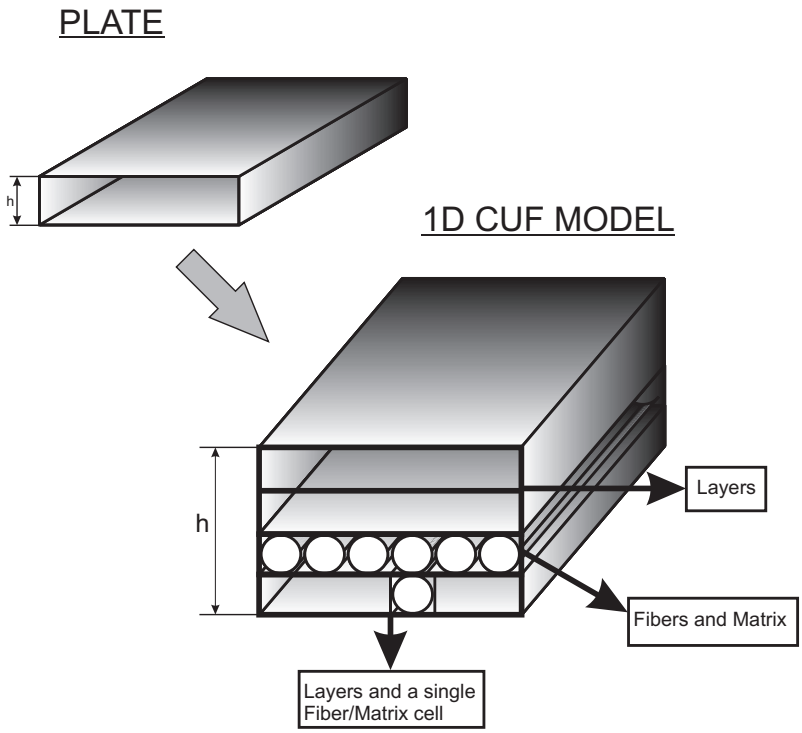

Figure 3.2. Component-wise approach to simultaneously model layers, fibers and matrices.

considered by means of the different modeling approaches offered by the present formulation. A composite C-shaped beam is analyzed as last numerical example. In order to be able to provide comparisons between different CW models, the material properties of laminae were retrieved from those of the constituent fibers and matrices by means of the Rule of Mixtures. For each case study, ANSYS solid models built with Solid95 elements, are used for comparison. Isotropic materials were chosen for the preliminary assessments in order to provide straightforward comparisons with solid models. This approach allow to refine the model just in determinate areas keeping the model light and, at the same time, obtaining an accurate description of the stress and strain fields where deemed necessary. Then, given the stress and strain distribution, failure criteria can be taken into account to perform failure analysis.

3.3 Single Cell Analysis

This section deals with the analysis of a single cell structure that is geometrically similar to a fiber/matrix cell in order to assess the simplest structural layout. Two modeling approaches were analysed. In the first model, the cell was treated as a homogeneous structure, in the second model the fiber and matrix were modeled separately. The material properties are reported in Table 6.5 where the first column refers to the homogeneous model while the second and third columns refer to the fiber/matrix cell.

	Homogeneous	Fiber	Matrix
	Material Properties		
E [GPa]	127.6	250.6	3.252
ν [-]	0.3	0.2456	0.355
	Failure Coefficients		
	Maximum Stress [MPa]		
X^T	1730	3398.1	66.5
X^C	1045	2052.6	255
S^L	95.1	186.8	74
	Maximum Strain [-]		
ε^T	0.0138	0.0138	0.00436
ε^C	0.01175	0.01175	0.002
γ^L	0.002	0.004	0.0016

Table 3.1. Material properties and failure coefficients.

3.3.1 Homogeneous Single Cell Analysis

The homogeneous cell is square with side $h = 0.1\ mm$, and $L/h = 10$ where L is the longitudinal length of the structure. The structure is clamped at $y = 0$ while a vertical point load, $F_z = -0.1$ N, was applied at [$h/2$, L, 0]. Results were obtained by means of TE models with different expansion order N and 40 B4 elements along the y-axis. Figure 5.6 shows three different meshes with one, four and sixteen nine-point elements (L9), for the LE cross-section model and a 10 B4 mesh was used along the beam axis.

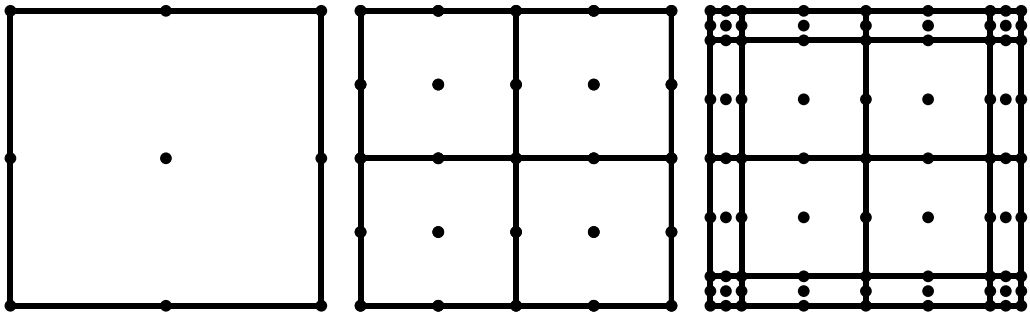

Figure 3.3. Model descriptions: 1 L9, 4 L9, 16 L9.

Table 3.2 presents the results obtained in terms of transverse displacement, u_z, at loading point in the homogeneous case study. The number of degrees of freedom (DOFs) of each model is shown in the last column of the table. The σ_{yy} and σ_{yz} trends above the cross section at $x = h/2$ are compared with solid results in Figure 3.4 at two different beam sections $y = 0$ and $y = L/2$.

3.3.2 Single Fiber/Matrix Cell Analysis

The CW geometry is depicted in Figure 3.5 for the fiber/matrix case study. The fiber diameter is $d = 0.08\ mm$, while other characteristic dimensions are the same to the homogeneous cell. The LE mesh is shown in Figure 3.6, it is composed of 12 L9 and 8 L6 elements. Transversal displacement u_z at loading point is shown in Table 3.3 and the axial and shear stress at points B[$b/2$,$L/2$,$d/2$] and D [d,$L/2$,0], B' [b/2,0,d/2] and D' [d,0,0] are reported in Table 3.4. Results above the clamped cross-section in terms of axial and shear stress in solid, LE and TE models are depicted in Figure 3.7 and 3.8.

Furthermore, strains above the clamped cross-section of the solid and LE models are compared in Figure 3.9. The corresponding strain values at points B' and D' are listed in Table 3.5.

A further assessment for a one single fiber/matrix cell is hereafter provided. In this case, the cylindrical component's Young modulus, E, is equal to 202.038 GPa and the Poisson ratio, ν, is equal to 0.2128. The surrounding portion of the structure was also considered isotropic with $E = 3.252$ GPa and $\nu = 0.355$. The structure is clamped at $y = 0$ while a vertical point load, $F_z = -0.1$ N, was applied at [$b/2$, L, 0]. Results were obtained by means of TE, LE and solid models. In case of TE, a 40 B4 mesh along the y-axis was

Model	$u_z \times 10^2[mm]$	DOFs
Classical Beam Model		
EBBT	−3.135	363
TBT	−3.155	605
TE		
N=1	−3.155	1089
N=2	−3.129	2178
N=3	−3.134	3630
N=4	−3.137	5445
N=5	−3.138	7623
N=6	−3.139	10164
N=7	−3.139	13068
N=8	−3.140	16335
LE		
1 L9	−3.126	837
4 L9	−3.136	2325
16 L9	−3.137	7905
SOLID		
	−3.154	210483

Table 3.2. Displacement of the single cell homogeneous model at the loading point.

Model	$u_z \times 10^2[mm]$	DOFs
Classical Beam Model		
EBBT	−6.356	363
TBT	−6.376	605
TE		
N=1	−6.376	1089
N=2	−6.335	2178
N=3	−6.338	3630
N=4	−6.345	5445
N=5	−6.345	7623
N=6	−6.349	10164
N=7	−6.349	13068
N=8	−6.350	16335
LE		
12 L9 + 8 L6	−6.440	7533
SOLID		
	−6.357	268215

Table 3.3. Displacement for the single cell CW model at the loading point.

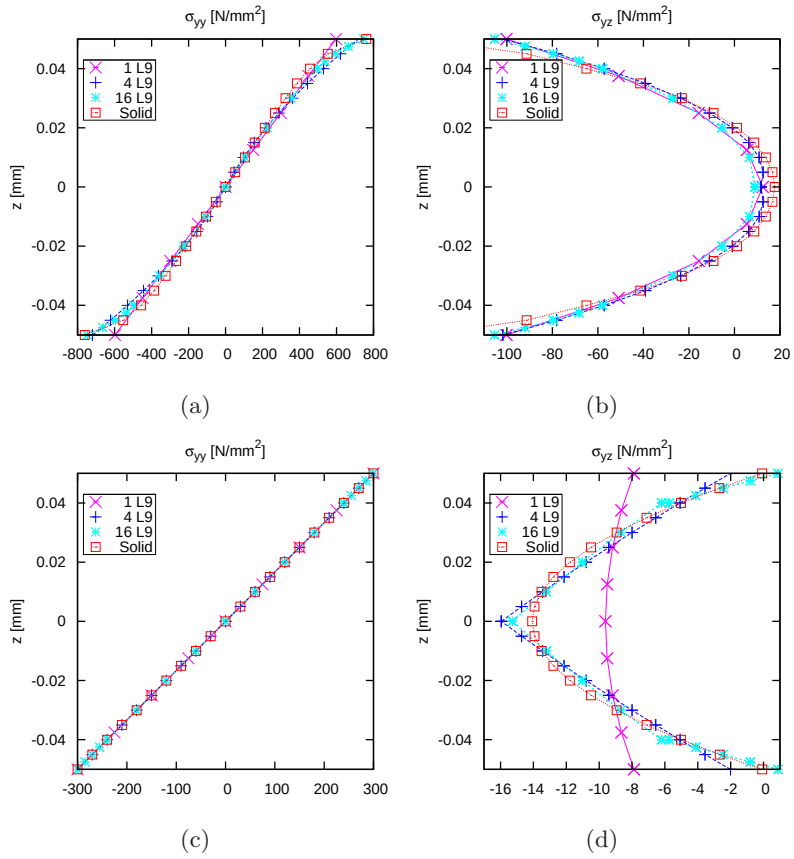

Figure 3.4. Stress distribution for the homogeneous cell: (a) Axial Stress σ_{yy} at $x = h/2$, $y = 0$, (b) Shear stress σ_{yz} at $x = h/2$, $y = 0$, (c) Axial Stress σ_{yy} at $x = h/2$, $y = L/2$, (d) Shear Stress σ_{yz} at at $x = h/2$, $y = L/2$.

Model	$\sigma_{yy} \times 10^{-2}$	$\sigma_{yz} \times 10^{-1}$	$\sigma_{yz} \times 10^{-2}$	
	Point B	Point D	Point B'	Point D'
Classical Beam Model				
EBBT	9.558	–	–	–
TBT	9.558	−1.966	-0.196	-0.196
TE				
N=1	9.558	−1.966	-0.196	-0.196
N=2	9.487	−2.353	-4.965	2.051
N=3	9.487	−2.481	-4.820	2.009
N=4	9.447	−2.475	-5.291	2.395
N=5	9.447	−2.407	-5.257	2.399
N=6	9.431	−2.406	-5.258	2.355
N=7	9.431	−2.348	-5.236	2.354
N=8	9.455	−2.348	-5.172	2.307
LE				
12 L9 + 8 L6	9.451	−2.551	-2.644	1.669
SOLID				
	9.531	−2.428	-2.423	1.797

Table 3.4. Stress values $[N/mm^2]$ for the single cell CW model at Point B,D ($y = L/2$) and Point B',D' ($y = 0$).

Model	$\varepsilon_{yz} \times 10^3$	
	Point B	Point D
Classical Beam Model		
EBBT	-	-
TBM	-0.195	-0.195
TE		
N=1	-0.195	-0.195
N=2	-4.935	2.038
N=3	-4.791	1.996
N=4	-5.259	2.381
N=5	-5.225	2.385
N=6	-5.226	2.341
N=7	-5.204	2.339
N=8	-5.140	2.294
LE		
	-2.669	1.756
SOLID		
	-2.409	1.786

Table 3.5. Strain values for the CW cell model at $y = 0$.

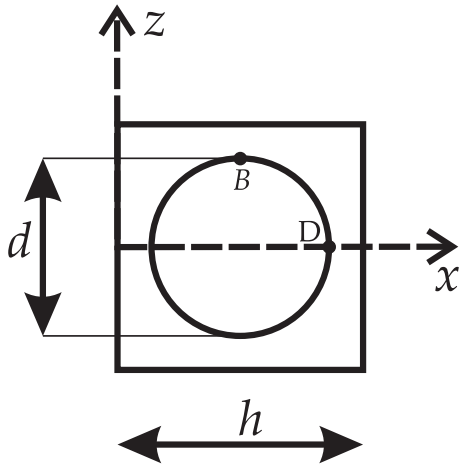

Figure 3.5. CW cell geometry.

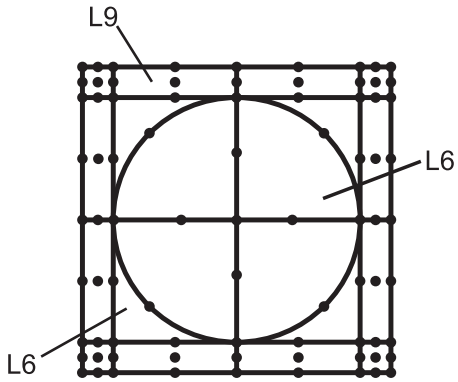

Figure 3.6. LE Element distribution: 12 nine-point (L9) elements and 8 six-point (L6) elements.

adopted. The LE cross-section discretization is shown in Figure 3.6, in this case, a 10 B4 mesh was used. The solid model was implemented in ANSYS.
Table 3.6 and 3.7 respectively presents the results obtained in terms of transverse displacement (u_z) and axial stress (σ_{yy}). u_z was evaluated at the loading point while σ_{yy} was evaluated at Point A[$b/2$, $L/2$, $d/2$] and Point B[$b/2$, $L/2$, 0.03], trasversal stress σ_{yz} was evaluated at Point C[0.01, $L/2$, $d/2$]. The last column of the Table 3.6 shows the number of degrees of freedom (DOFs) of each model. The analysis of the results leads to the following considerations:

1. There is a general good agreement between the proposed model and the solid model solutions for the homogeneous and fiber/matrix cell;

2. For the homogeneous cell, the maximum value of σ_{yy} is reached at Point A'[h/2, 0, h] where the 1 L9 mesh is not able to catch the solid results, this implies the need for refined meshes. Moreover a refined mesh is required to provide the shear stress

Model	$u_z \times 10^2$ Loading Point mm	DOFs
	Classical Beam Model	
EBBT	−7.811	363
TBT	−7.835	605
	TE	
$N = 1$	−7.835	1089
$N = 2$	−7.774	2178
$N = 3$	−7.777	3630
$N = 4$	−7.794	5445
$N = 5$	−7.795	7623
$N = 6$	−7.800	10161
$N = 7$	−7.800	13068
$N = 8$	−7.804	16335
	LE	
12 L9 + 8 L6	−7.933	7533
	SOLID	
	−7.818	268215

Table 3.6. Displacement values for the single cell model.

Model	σ_{yy} Point A $\times 10^{-2}$ MPa	σ_{yy} Point B	σ_{yz} Point C $\times 10^{-1}$ MPa
	Classical Beam Model		
EBBT	9.469	7.102	−1.962
TBT	9.469	7.102	−1.962
	TE		
$N = 1$	9.469	7.102	−1.962
$N = 2$	9.358	7.019	−2.311
$N = 3$	9.358	7.019	−2.464
$N = 4$	9.327	7.090	−2.454
$N = 5$	9.327	7.090	−2.375
$N = 6$	9.315	7.105	−2.373
$N = 7$	9.315	7.105	−2.304
$N = 8$	9.346	7.117	−2.301
	LE		
12 L9 + 8 L6	9.450	7.046	−2.500
	SOLID		
	9.492	7.094	−2.383

Table 3.7. Stress values for the single cell model.

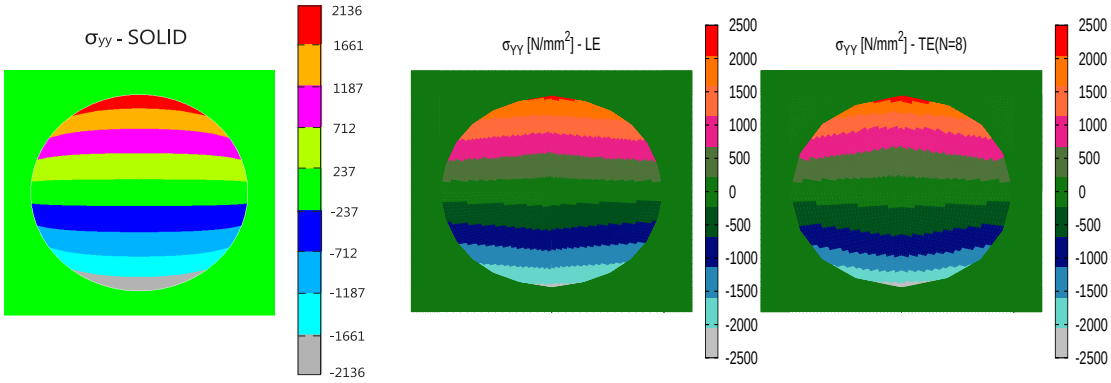

Figure 3.7. Axial stress at the clamped cross-section.

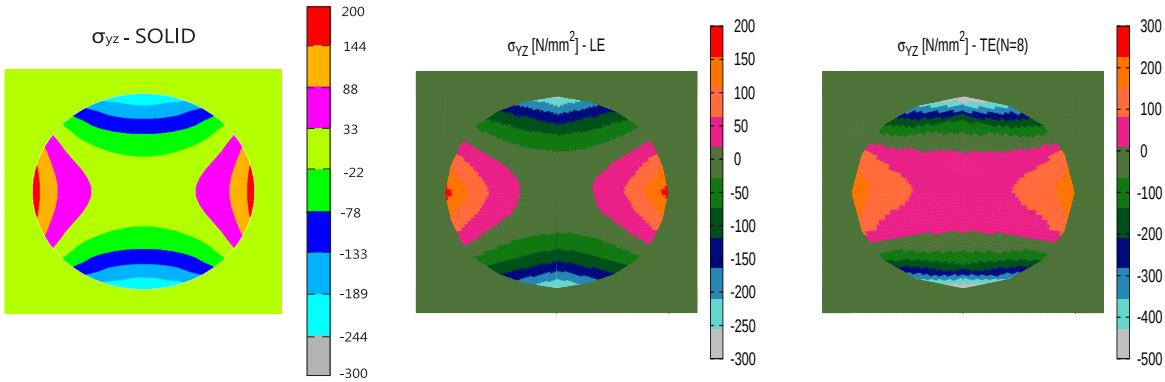

Figure 3.8. Shear stress at the clamped cross-section.

distribution, σ_{yz}, at y=L/2. The 4 L9 and 16 L9 meshes used are able to provide the needed improvement;

3. The Component-Wise model provides a refined description of the stress/strain field of the cell, in particular it gives a good description of the interfaces;

4. At the clamped cross-section the LE models provide better results than TE models;

5. The computational costs of the proposed 1D models are far lower than those required for the solid model.

3.4 Double Cell Analysis

A double cell model is examined in this section. A graphic description of the cross-section geometry is provided in Figure 3.10 while in Figure 3.11 a 3D view of the case study is shown. The characteristic dimensions are $b = 0.1\ mm$, $a = 0.2\ mm$ and $L/b = 10$ where

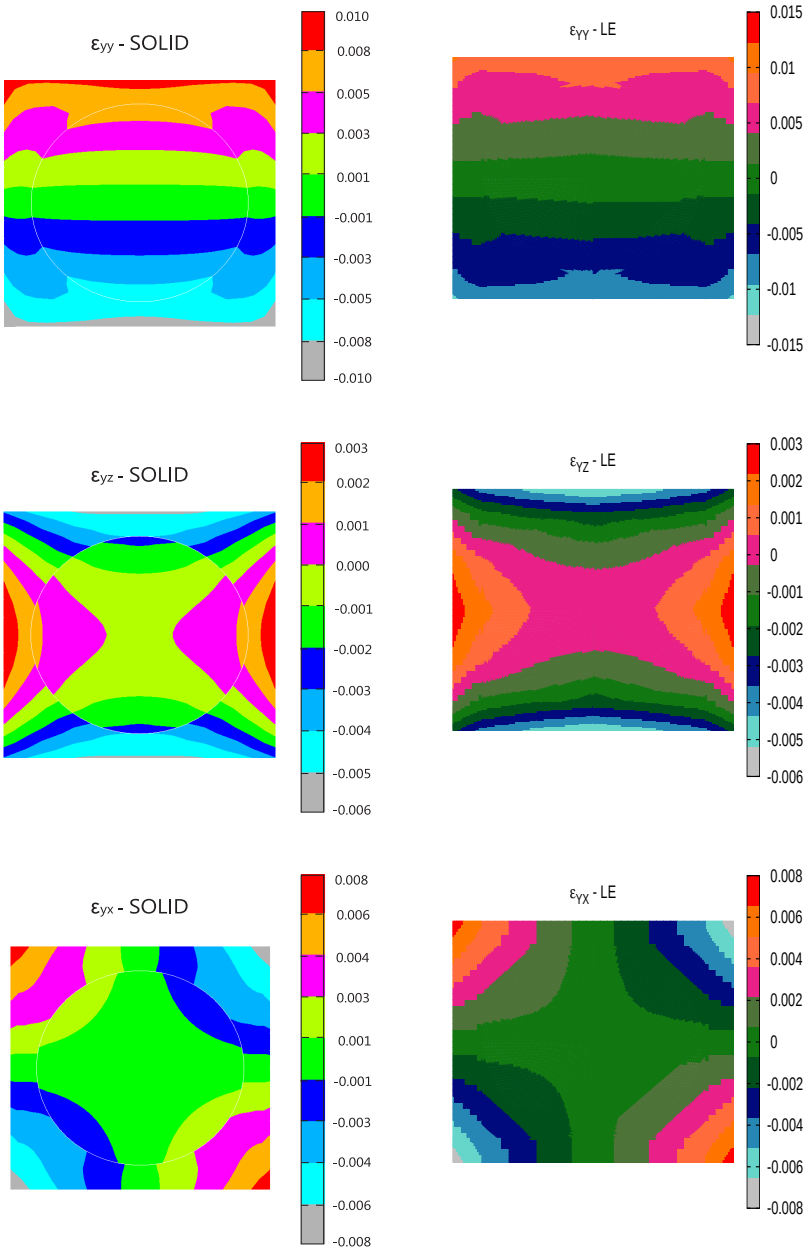

Figure 3.9. Axial ε_{yy} and shear ε_{yz}, ε_{yx} strain at $L = 0$ for the Solid and LE CW cell models.

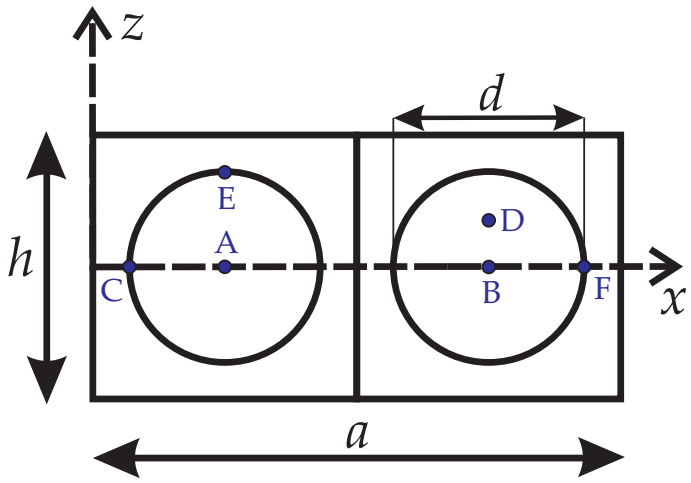

Figure 3.10. Double cell geometry.

L is the longitudinal length of the structure. The fiber diameter is $d = 0.08\ mm$, as in the previous single cell case study. Results were obtained by means of TE, LE and solid models. The LE mesh is composed of 20 $L9$ and 16 $L6$ elements above the cross-section, 10 B4 elements are employed along the y-axis while 40 B4 elements are used for the TE model. The structure was clamped at $y = 0$ while two vertical point loads, $F_z = -0.02$ N, were applied at the center of each cell. Table 3.8 presents the results obtained in terms

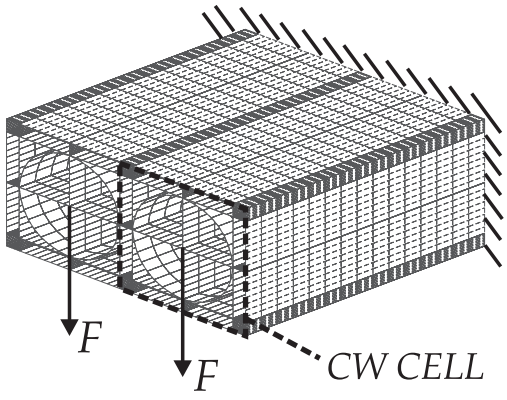

Figure 3.11. Double cell case study.

of transverse displacement, u_z, at [a/2, L, h/2], the last column shows the number of degrees of freedom (DOFs) of each model. Table 3.9 shows axial and shear stress, σ_{yy} and σ_{yz}, at points E [a/4, L, h/2] and F [a/2+d, L, h/2] and their corresponding points at clamped cross-section E'[a/4, 0, h/2] and F'[a/2+d, 0, h/2]. Figure 3.13 depicts the stress distribution above the clamped cross-section for the LE, TE (N=8) and the solid model. Increasing the two vertical point loads, $F_z = -0.05$ N, applied at Point A [$a/4$, L, $h/2$]

Model	$u_z \times 10^2[mm]$	DOFs
Classical Beam Model		
EBBT	−1.271	363
TBT	−1.275	605
TE		
N=1	−1.275	1089
N=2	−1.259	2178
N=3	−1.260	3630
N=4	−1.262	5445
N=5	−1.263	7623
N=6	−1.264	10164
N=7	−1.264	13068
N=8	−1.265	16335
LE		
20 L9 + 16 L6	−1.285	12555
SOLID		
	−1.268	536430

Table 3.8. Displacement of the double cell CW model at [a/2,L,h/2].

Model	$\sigma_{yy} \times 10^{-2}$ Point E	σ_{yz} Point F	$\sigma_{yy} \times 10^{-2}$ Point E'	σ_{yz} Point F'
Classical Beam Model				
EBBT	1.912	–	3.823	-
TBT	1.912	−3.933	3.823	-3.933
TE				
N=1	1.912	−3.933	3.823	-3.933
N=2	1.897	−6.636	3.814	6.489
N=3	1.897	−7.347	4.417	6.383
N=4	1.878	−7.312	4.402	5.014
N=5	1.878	−6.834	4.375	5.137
N=6	1.879	−6.864	4.343	7.064
N=7	1.879	−6.611	4.513	7.072
N=8	1.889	−6.575	4.511	6.303
LE				
20 L9 + 16 L6	1.909	−6.277	4.317	4.360
SOLID				
	1.905	−6.034	4.263	4.404

Table 3.9. Stress values $[N/mm^2]$ for the double cell CW model at Point E,F ($y = L/2$) and Point E',F' ($y = 0$).

and Point B $[3a/4, L, h/2]$. Table 3.10 presents the results obtained in terms of transverse

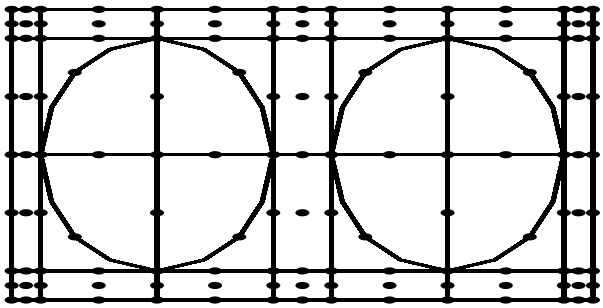

Figure 3.12. L9 + L6 distribution of the double cell cross-section.

displacement u_z at loading points. Table 3.11 shows the axial (σ_{yy}) and transversal (σ_{yz}) stress respectively evaluated at Point C [0.01, 0, 0], D [$3a/4$, $L/2$, 0.03] and E[$a/4$, $L/2$, 0.04]. The results are evaluated in terms of displacements, stress/strain fields. Three

Model	$u_z \times 10^2$ Point A,B mm	DOFs
Classical Beam Model		
EBBT	−3.906	363
TBT	−3.917	605
TE		
$N = 1$	−3.917	1089
$N = 2$	−3.868	2178
$N = 3$	−3.869	3630
$N = 4$	−3.879	5445
$N = 5$	−3.879	7623
$N = 6$	−3.885	10161
$N = 7$	−3.885	13068
$N = 8$	−3.887	16335
LE		
20 L9 + 16 L6	−3.958	12555
SOLID		
	−3.901	536430

Table 3.10. Displacement values for the double cell model.

main cell configurations were investigated under point loads. Comparisons with solid models from the FEA (Finite Element Analysis) ANSYS commercial code were proposed. Failure analyses were conducted taking into account Maximum Stress and Maximum Strain criteria. The analysis of the results leads to the following considerations:

1. The CW approach allows the modelling of a fiber-reinforced composite structure. Approximations introduced by the homogenization theories are avoided;

2. As in the previous cases there is a general good agreement with solid and CW results;

Model	σ_{yy} Point E $\times 10^{-2}$ MPa	σ_{yy} Point F	σ_{yz} Point C $\times 10^{-1}$ MPa
	Classical Beam Model		
EBBT	4.734	3.551	−0.981
TBT	4.734	3.551	−0.981
	TE		
$N = 1$	4.734	3.551	−0.981
$N = 2$	4.679	3.509	−1.591
$N = 3$	4.679	3.509	−1.771
$N = 4$	4.625	3.513	−1.759
$N = 5$	4.625	3.513	−1.655
$N = 6$	4.641	3.552	−1.670
$N = 7$	4.641	3.552	−1.590
$N = 8$	4.664	3.556	−1.583
	LE		
20 L9 + 16 L6	4.647	3.522	−1.584
	SOLID		
	4.744	3.546	−1.519

Table 3.11. Stress values for the double cell model.

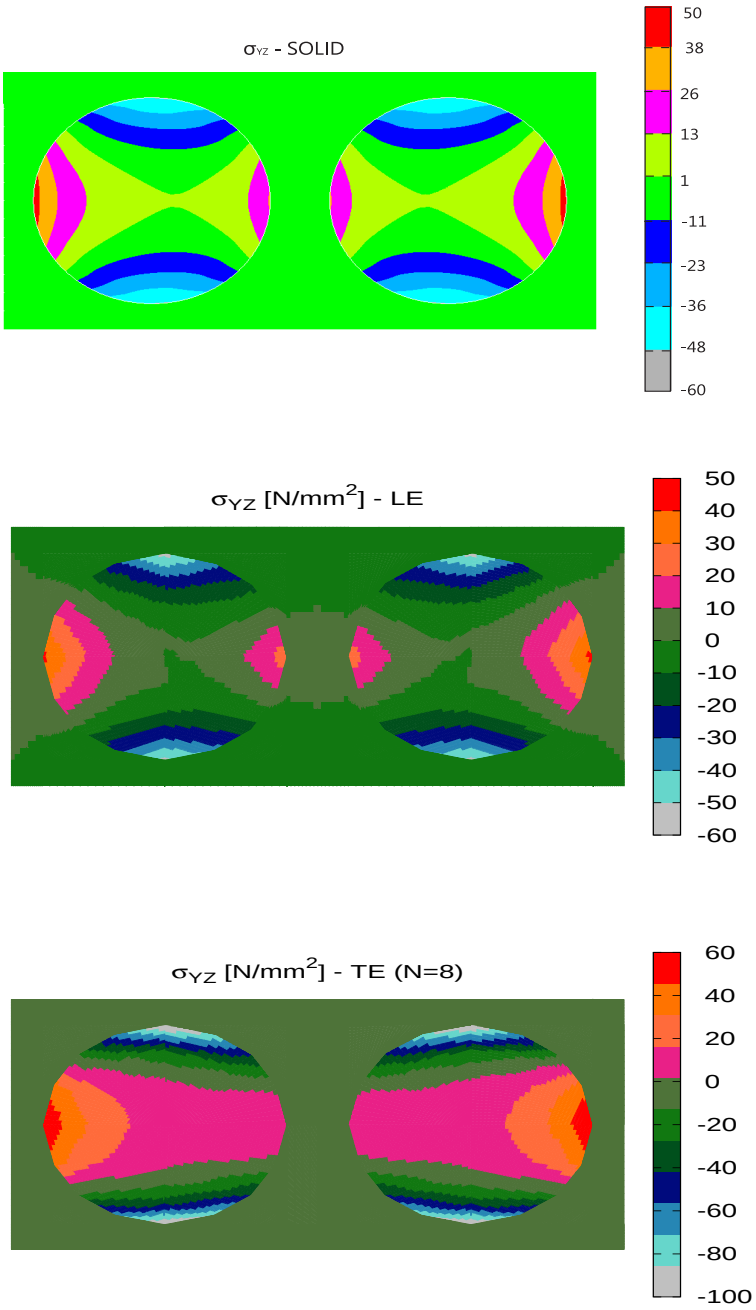

Figure 3.13. Shear stress σ_{yz} at the clamped cross-section. Double cell Solid and CW models.

3. The LE model provides the best convergence of axial and shear stress to solid results while the TE model requires a high order, N, to provide good convergence at the clamped cross-section;